Seawater Lead Isotopes Record Early Miocene to Modern Circulation Dynamics in the Pacific Sector of the Southern Ocean

Huang Huang[1,2,3,4], **Marcus Gutjahr[1]**, **Zhaoyang Song[4,5]**, **Jan Fietzke[1]**, **Martin Frank[1]**, **Gerhard Kuhn[6]**, **Claus Dieter Hillenbrand[7]**, **Marcus Christl[8]**, **Dieter Garbe-Schönberg[9,10]**, **Tyler Goepfert[11]**, and **Anton Eisenhauer[1]**

[1]GEOMAR Helmholtz Centre for Ocean Research Kiel, Kiel, Germany, [2]Laboratory for Marine Geology, Qingdao Marine Science and Technology Center, Qingdao, China, [3]School of Marine Sciences, Sun Yat-Sen University, Zhuhai, China, [4]Southern Marine Science and Engineering Guangdong Laboratory (Zhuhai), Zhuhai, China, [5]School of Atmospheric Sciences, Sun Yat-Sen University, Zhuhai, China, [6]Alfred-Wegener-Institut Helmholtz-Zentrum für Polar- und Meeresforschung, Bremerhaven, Germany, [7]British Antarctic Survey, Cambridge, UK, [8]ETH Zurich, Laboratory of Ion Beam Physics, Zurich, Switzerland, [9]Institute for Geosciences, Christian-Albrechts-University, Kiel, Germany, [10]Department of Physics and Earth Sciences, Jacobs University Bremen gGmbH, Bremen, Germany, [11]School of Earth and Space Exploration, Arizona State University, Tempe, AZ, USA

Abstract The Antarctic Circumpolar Current (ACC) is Earth's largest current flowing around Antarctica at all depths and connecting major ocean basins, thus representing an important component of Earth's climate. However, the timing and key controls determining ACC flow path and its strength as a function of past climatic boundary conditions that ultimately resulted in its modern configuration remain unclear due to major uncertainties in paleoceanographic and tectonic reconstructions. Here we present a unique high-resolution laser ablation-derived late Cenozoic seawater lead isotope record obtained from a hydrogenetic ferromanganese crust from the Pacific sector of the Southern Ocean. Our Pb isotope data reveal that the ACC has experienced five stable circulation states since the early Miocene which were separated by four major transitions observed at 17.5-14.6, 12, 10 and 5 Ma. We suggest that the relatively abrupt transitions between ACC circulation state were mainly induced by tectonic changes, whereas the impact of climatic changes was of secondary importance. According to our data the modern ACC configuration formed 5 million years ago, likely in response to the closure of the Panama Seaway. Since the Drake Passage (DP) has already been an open seaway since at least the late Miocene, our results demonstrate that DP opening was not the only factor affecting past ACC circulation. Our data also show that changes in the latitudinal position of the ACC were linked to the middle Miocene waxing and waning of the Antarctic ice sheets, which emphasizes the ACC's critical role as a key control of Antarctic glaciation.

1. Introduction

The Antarctic Circumpolar Current (ACC) is the largest current on Earth in terms of volume transport. Its core corresponds to the latitudinal position of the maximum strength of the westerlies and its clockwise circumpolar flow is unimpeded by land barriers. The ACC is the only current connecting all major oceans, that is, Atlantic, Pacific and Indian Oceans. The inter-basin connection of the ACC is playing a critical role in the global transport and distribution of heat, salt and gases (e.g., carbon dioxide, CO_2), thus intimately linking it to Earth's climatic changes (Gordon, 2001).

Despite the profound importance of the modern ACC on the global climate system, it remains equivocal when and how it evolved into its modern configuration. The initiation and subsequent evolution of the ACC is widely thought to have been dominated by the progressive tectonic opening of two Southern Ocean (SO) seaways, that is, the Tasman Gateway (TG) between Australia and East Antarctica and the Drake Passage (DP) between South America and the Antarctic Peninsula (Kennett, 1977) (Figure 1, inset). The deepening of the TG began at around 35.5 Ma and ended at about 30.2 Ma, while the tectonic evolution of the DP was more complex (Scher et al., 2015; Stickley et al., 2004). Evidence for its initial opening was found at approximately 41 Ma allowing the first shallow Pacific seawater inflow into the Atlantic sector of the SO (Scher & Martin, 2006). Age estimates for the onset of a deep Pacific-Atlantic connection vary substantially, ranging from as early as the Eocene-Oligocene Transition
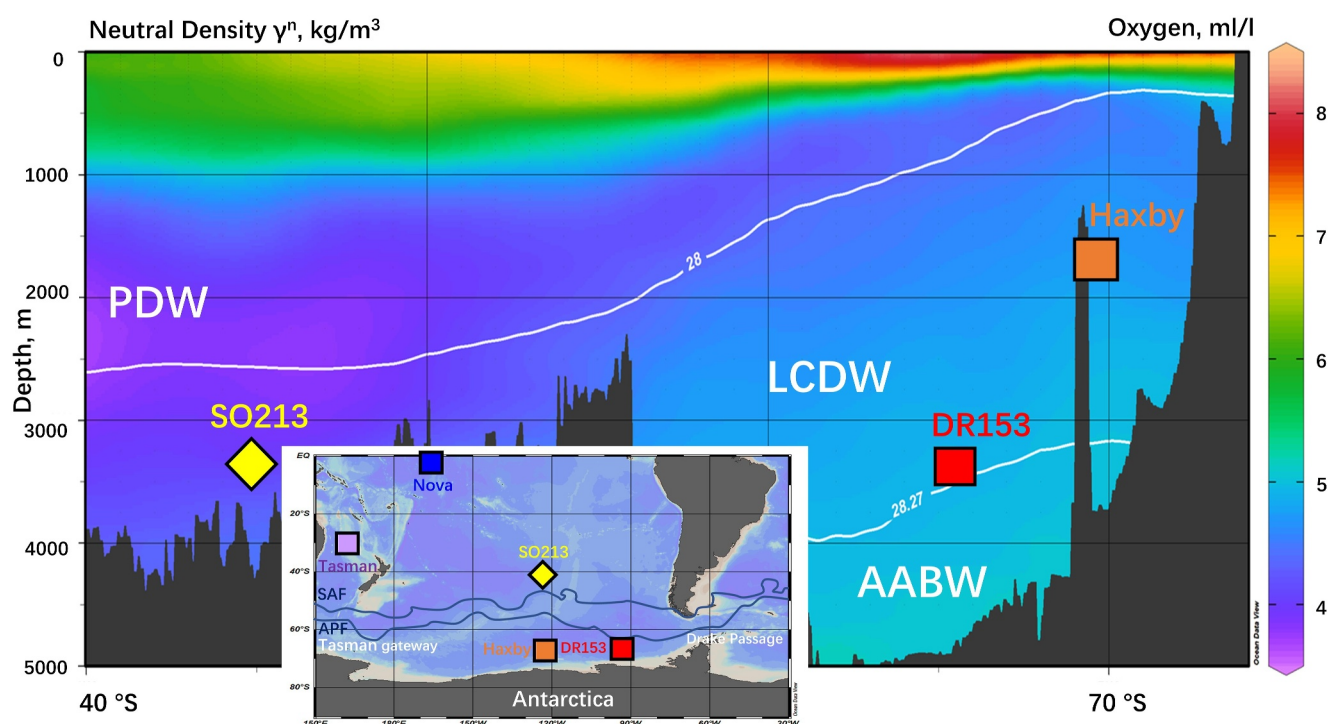
Figure 1. Sample locations and the modern hydrography of the Pacific sector of the Southern Ocean. Color-mapped oxygen concentrations, with neutral density contours (γ^n) overlain, as drawn from the 2013 World Ocean Atlas (Garcia et al., 2013; Zweng et al., 2013). Sampling sites of ferromanganese crusts Haxby, DR153 (Frank et al., 2002), Tasman (van de Flierdt et al., 2004) and Nova (van de Flierdt et al., 2004) are shown as filled rectangles, and sediment core site SO213 (Molina-Kescher et al., 2016) is shown as a filled diamond alongside the Antarctic Polar Front and Subantarctic Front (Orsi et al., 1995). The isopycnal with a neutral density of 28.27 kg m^{-3} defines the water mass boundary between AABW and Lower Circumpolar Deep Water (LCDW), while the 28.00 kg m^{-3} isopycnal defines the top of LCDW as defined in an earier study (Orsi et al., 1995, 1999). Figure created with Ocean Data View (Schlitzer, 2011). AABW: Antarctic Bottom Water; LCDW: Lower Circumpolar Deep Water; PDW: Pacific Deep Water.

(Livermore et al., 2005) to the Miocene (Barker, 2001; Dalziel et al., 2013; Riley et al., 2021). Tectonic reconstructions and grain size data from marine sediments suggested that an ACC configuration similar to the modern may already have formed in the Oligocene (Lawver & Gahagan, 2003; Pfuhl & McCave, 2005). However, recent reconstructions of the provenance and chemical composition of SO deep water using authigenic neodymium (Nd) isotope compositions suggest that a circumpolar current like that of today did not exist before the late Miocene (Evangelinos et al., 2022, 2024). Yet to date, there is no continuous circulation reconstruction that provides insights into the detailed ACC evolution from early Miocene to today due to the scarcity of sedimentary records from the Pacific sector of the SO.

The isotopic composition of dissolved lead (Pb) in seawater is a highly sensitive tracer of regional water mass sourcing and mixing (Frank, 2002). Lead has three radiogenic isotopes, that is, ^{206}Pb, ^{207}Pb and ^{208}Pb produced from the decay of ^{238}U, ^{235}U and ^{232}Th, and one primordial isotope ^{204}Pb, thus allowing combination of multiple Pb isotopic ratios, for example, ^{206}Pb/^{204}Pb and ^{208}Pb/^{206}Pb, for sensitive identification of individual water masses. Fluvial input was the main source of Pb to seawater prior to the industrial revolution, so variable and regionally distinct seawater Pb isotopic compositions are acquired from the weathering of continental rocks of different ages and ratios between daughter and parent isotope abundances (Chen et al., 2023; Frank, 2002). Due to the long half-lives of ^{238}U (T$_{1/2}$ = 4.47 Gyr), ^{235}U (T$_{1/2}$ = 0.704 Gyr) and ^{232}Th (T$_{1/2}$ = 14 Gyr), the impact of radioactive decay on Pb isotopic compositions after precipitation in hydrogenetic marine phases are negligible on time scales of few million years. The high particle-reactivity of Pb results in a short residence time of this trace metal in the deep ocean (50–200 years) (Cochran et al., 1990; Henderson & Maier-Reimer, 2002; Schaule & Patterson, 1981). Compared to seawater Nd isotopes, the advantage of using Pb isotopes as a water mass tracer is that its short residence time allows formation of distinct Pb isotopic compositions in the three major SO basins (Abouchami & Goldstein, 1995), thus providing detailed water mass mixing and provenance information, whereas modern Nd isotope compositions around Antarctica are well mixed and show similar values (van de

Flierdt et al., 2016). Dissolved Pb in seawater, likely often present as colloids rather than in truly dissolved form (Marsay et al., 2018), is efficiently scavenged throughout the water column due to its particle-reactivity. Upper water column derived Pb can be transported to the deep ocean with sinking particles resulting in the deep water Pb isotopic signal reflecting the integrated composition of the entire water column (Huang et al., 2020; Lanning et al., 2023; Wu et al., 2010).

In this study, we employ a laser ablation-based multiple-collector inductively plasma mass spectrometry (LA-MC-ICPMS) technique (Christensen et al., 1997) to generate an unprecedented continuous high-resolution seawater Pb isotope record for the past 20 Myr from ferromanganese crust PS75/247-2 (hereafter called "Haxby") dredged on the southern flank of Haxby Seamount (Kipf et al., 2014) in the Pacific sector of the SO (Figure 1). Our new data provide critical insights into past ACC dynamics in the Pacific sector since the early Miocene. Forcing factors, including orbital parameters, tectonic evolution, and variability in Antarctic ice sheet volume, have been suggested to affect ACC flow, thus we employ the Kiel Climate Model (KCM) to examine these potential triggers of ACC changes found in our record.

Ferromanganese crust Haxby was recovered from Haxby Seamountpart of the Marie Byrd Seamounts located in the western Amundsen Sea, north of the continental shelf of Marie Byrd Land, West Antarctica (Figure 1). Radiometric ages and geochemical data suggest that the Marie Byrd Seamounts were formed by the adiabatic rise of HIMU (=high $^{238}U/^{204}Pb$) mantle material from the base of Marie Byrd Land due to the crustal extension at the southern boundary of the Bellingshausen Plate from about 74 to 62 Ma (Kipf et al., 2014). Crust Haxby, situated in the central Pacific sector of the SO, is ideally positioned to record deep ocean circulation changes in response to the tectonic evolution of the DP to the east and the TG to the west.

The modern ACC is a deep-reaching current stretching from the sea surface to the SO seafloor (Carter et al., 2008; Rintoul, 2018) and its meridional circulation can be generally characterized as a two-cell overturning system, including "upper" and "lower" cells (Gordon, 2001; Lumpkin & Speer, 2007; Talley, 2013). In the lower cell, westerly wind-driven upwelling brings Circumpolar Deep Water (CDW), the major ACC water mass, to the surface south of Antarctic Polar Front (APF). Part of the upwelled deep water moves southwards to the Antarctic continental margin and sinks in several distinct shelf regions to form new Antarctic Bottom Water (AABW) that returns to the deep SO (Purkey et al., 2018; Solodoch et al., 2022). In the upper cell, the other part of the upwelled water is subducted and moves northwards at shallower depths to leave the SO in the form of either Antarctic Intermediate Water or Subantarctic Mode Water (Rintoul, 2018; Talley, 2013). Currently, crust Haxby is bathed in Lower Circumpolar Deep Water (LCDW), while northern-sourced Pacific Deep Water (PDW) only mixes with the less dense Upper Circumpolar Deep Water (UCDW).

The natural seawater Pb isotope signal prior to the industrial era can be recovered from ferromanganese nodules/ crusts (Klemm et al., 2007), despite that today the global seawater Pb isotope signal is overwhelmed by anthropogenic inputs, for example, in the North Pacific and the Amundsen Sea (Ndungu et al., 2016; Wu et al., 2010). Previous surveys of Pleistocene surface scrapings on ferromanganese nodules have identified three distinct regional Pb isotope endmembers in the South Pacific and the SO's Pacific sector (Abouchami & Goldstein, 1995; von Blanckenburg et al., 1996) which are approximated here by the arrays "West Antarctic," "East Antarctic," and "Pacific" (Figure 2). The benefit of using a combination of two radiogenic isotope compositions of Pb is apparent in Figure 2, where the variability of seawater Pb isotope signatures as a function of water mass changes is illustrated. Among different paired Pb isotopic ratios, the combination of $^{208}Pb/^{206}Pb$ and $^{206}Pb/^{204}Pb$ shows the most distinct patterns for resolving variable water masses; thus, other ratios are only shown in the Supporting Information S1 and are not further discussed in this study. Modern observations have shown that AABW in the Pacific sector is mainly composed by two varieties: less voluminous Adélie Land Bottom Water (ALBW) and the more dominant Ross Sea Bottom Water (RSBW) (Purkey et al., 2018; Solodoch et al., 2022). The two ferromanganese nodules located close to the formation area of RSBW (Ross Sea (RS) in Figure 2) show a distinct RSBW signal with very low $^{208}Pb/^{206}Pb$ and intermediate $^{206}Pb/^{204}Pb$ ratios. Following the overall path of the ACC that flows eastward, the Pb isotope signatures of ferromanganese nodules gradually increase in $^{208}Pb/^{206}Pb$ and decrease in $^{206}Pb/^{204}Pb$ from the RS region to the Bellingshausen Sea (BS) region, and further to the DP and the SW Atlantic regions where the seawater Pb isotope signal is dominated by local weathering input from West Antarctica, the Antarctic Peninsula and Patagonia. Likewise, the two ferromanganese nodules from offshore Adélie Land (AL in Figure 2), that are bathed in a regional AABW variety with a high ALBW proportion (>60 vol.%) (Thomas et al., 2020), show a distinct ALBW signal with very high $^{206}Pb/^{204}Pb$ and intermediate

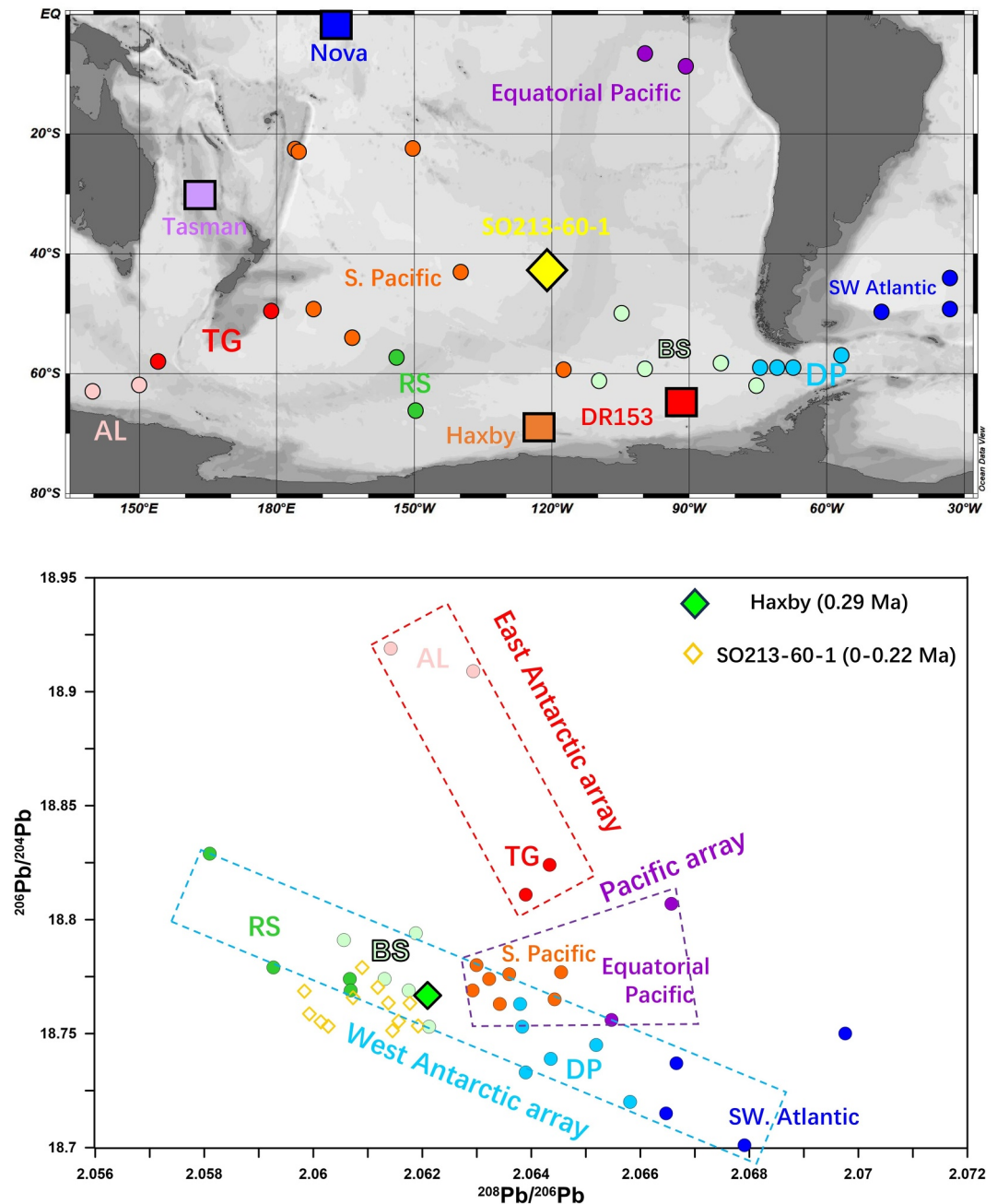**Figure 2.** Combined ^{206}Pb/^{204}Pb and ^{208}Pb/^{206}Pb ratios in the surface scrapings on ferromanganese nodules. In the upper map, the colored round dots, squares and diamond indicate the locations of ferromanganese nodules (Abouchami & Goldstein, 1995; von Blanckenburg et al., 1996), ferromanganese crusts (van de Flierdt et al., 2004) and sediment core SO213-60-1 (Molina-Kescher et al., 2016), respectively. In the lower panel, the colored round dots show the Pb isotopic compositions of ferromanganese nodules from different areas. For comparison, the Pleistocene Pb isotopic compositions of crust Haxby and authigenic phase in SO213-60-1 are indicated by different colored diamonds. RS: Ross Sea; AL: Adélie Land; S. Pacific: South Pacific; TG: Tasman Gateway; DP: Drake Passage; SW Atlantic: Southwest Atlantic; BS: Bellingshausen Sea.

^{208}Pb/^{206}Pb ratios likely originating from the weathering of old cratonic rocks in East Antarctica. As the proportion of ALBW decreases to ~30 vol.% when AABW is exported northwards into the Pacific Ocean (Solodoch et al., 2022), the ^{206}Pb/^{204}Pb and ^{208}Pb/^{206}Pb ratios in ferromanganese nodules from locations further north and at a large distance from AL (TG in Figure 2) shift toward the Pacific Pb isotopic endmember, which is recorded in
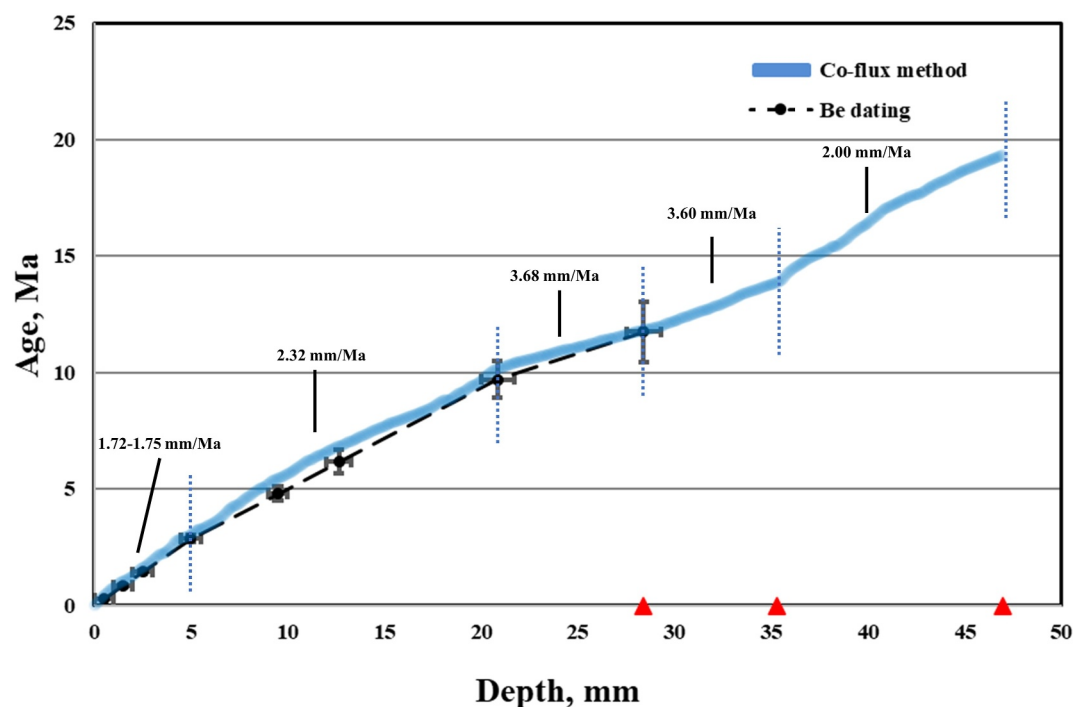
Figure 3. Calculated ages versus sample depth of crust Haxby. The $^{10}Be/^9Be$ dated ages were calculated with a half-life for ^{10}Be of 1.387 Myr by assuming a constant initial $^{10}Be/^9Be$ ratio. The growth rates and ages beyond the age range covered by $^{10}Be/^9Be$ dating have been calculated using a constant Co-flux/growth rate relationship (Manheim, 1986) which was calibrated to match the $^{10}Be/^9Be$ dating of the younger part. The dashed black lines represent the Be-derived age model. The solid blue line shows the Co-flux derived age model. The red triangles indicate the tie points for calculating Co-flux derived growth rates. The dashed bule lines are used to defined the section with different growth rates.

ferromanganese nodules from the South and equatorial Pacific. It is worth noting that Pb in the equatorial Pacific carries a unique isotope signal, which characterized by a higher $^{208}Pb/^{206}Pb$ ratio than RSBW and ALBW and a higher $^{206}Pb/^{204}Pb$ ratio than the local seawater Pb isotope signal recorded in DP. Therefore, our Pb isotope records most sensitively trace variable contributions of RSBW, ALBW and deep waters originating from the Pacific to LCDW.

2. Materials and Methods

2.1. Sample Collection and Preparation

Crust Haxby was dredged from Haxby Seamount at 69°08.16′–69°08.53′S and 123°12.76′–123°13.13′W and from a water depth of 1,502–1,734 m during expedition ANT-XXVI/3 in early 2010 with the German research vessel RV *Polarstern* (Gohl, 2010). The ferromanganese crust was first placed in epoxy before cutting. After each cut, the sample was embedded in epoxy resin again to preserve the sample structure. Eventually, an approximately 5 cm long, 2 cm wide, and 0.2 cm thick section of the sample (Figure S1 in Supporting Information S1) was cut following the main growth direction. The sample slide was polished using Buehler "Micropolish" (Buehler GmbH, Duesseldorf, Germany) before microprobe and LA-MC-ICPMS measurements were conducted.

2.2. Age Model

The age model (Figure 3) for crust Haxby is based on $^{10}Be/^9Be$ and high-resolution cobalt (Co) flux methods following van de Flierdt et al. (2004). For the last 11.75 Ma, the average crust growth rates and age–depth relationships were determined directly from the $^{10}Be/^9Be$ profile. Due to the ^{10}Be half-life of 1.387 Myr (Chmeleff et al., 2010), ^{10}Be concentrations at ages older than 11.75 Ma are not detectable any more (>8 half-lives), and the ages older than 11.75 Ma had to be estimated based on a Co-constant flux model (Frank et al., 1999; Manheim, 1986). The methods are detailed in the Supporting Information S1.

2.3. Pb Isotope Compositions Analyzed by LA-MC-ICP-MS

The Pb isotopic compositions were determined by laser ablation coupled to a MC-ICP-MS (LA-MC-ICP-MS) using an Analyte Excite Excimer Laser Ablation System connected to a Thermo Scientific Neptune Plus MC-ICP-MS at GEOMAR Kiel. The instrumental parameters of the LA-MC-ICP-MS are listed in Tables S5 and S6 in Supporting Information S1. After assessing the age-depth relationship in the uppermost 5 mm of crust Haxby, we used smaller laser spot sizes (each integrating about 8 kyr of growth) to resolve glacial-interglacial cyclic $^{206}Pb/^{204}Pb$ and $^{208}Pb/^{206}Pb$ variations in the youngest part of our record (Figures 4e and 4g). We also used larger laser spot sizes to integrate a sampling interval of approximately 40 kyr of growth (i.e., one early Pleistocene glacial cycle) in order to detect long term changes beyond orbital cyclicity throughout the past 20 Ma (Figures 4b, 4c, 5, and 6). In order to verify the laser ablation based Pb isotope data, the Pb isotope compositions of samples from 10 different depths in crust Haxby were also analyzed by conventional solution-based method. The detailed analytical protocols are described in the Supporting Information S1.

2.4. Numerical Experiments

We use the KCM (Park et al., 2009) to investigate the influence of changes in the oceanic gateways and Antarctic ice sheet volume on the ACC state. The KCM is a fully coupled atmosphere-ocean-sea ice general circulation model, which consists of the atmosphere model ECHAM5 and the ocean-sea ice model NEMO. In the version applied here, ECHAM5 (Roeckner et al., 2003) is used with a horizontal resolution of T31 ($3.75° \times 3.75°$) and 19 vertical levels reaching up to 10 hPa. This resolution is relatively coarse and unable to resolve the bathymetry in detail, but it is adequate to examine larger-scale circulation changes recorded in our seawater Pb isotope data set. The ocean-sea ice component NEMO (Madec et al., 2008) is run on a 2° Mercator mesh and with 31 vertical levels. An enhanced meridional resolution of 0.5° is used in the equatorial region. The two models are coupled with the OASIS3 coupler (Valcke, 2006). Our model provides the simulation results for water depths at 1,410 m and 1,830 m, which bracket the depth range of crust Haxby (1,502–1,734 m). The modeling results at 1,410 m and 1,830 m in the investigated area are almost identical (Figure S5 in Supporting Information S1), indicating that the difference in circulation for this depth interval is negligible. We focused on the simulation at 1,410 m depth because it is slightly closer to the water depth range of crust Haxby. We also show the simulation results at 3,260 m water depth which is consistent with the water depths of the location of ferromanganese crust DR153 from the DeGerlache Seamounts in the BS (Frank et al., 2002) (Figure 7 and Figure S7 in Supporting Information S1).

Five simulations were performed: a 4,500-year-long present-day control run (PRES) that is initialized with the Levitus temperature and salinity climatology. The Levitus data set provides long-term means of objectively analyzed ocean temperature and salinity at multiple water depths (Conkright et al., 1998). The PRES simulation employs the CO_2 concentration in 2017 (405 ppm), modern land-sea mask, orography and continental ice-sheet configuration (Song et al., 2017).

In the other 3,500-year-long simulation (PLIO) (Song et al., 2017), an open Panama Seaway is implemented by replacing four land grids with ocean grids, while the settings for the land-sea mask, the Antarctic ice sheet, greenhouse gases, etc., are the same as in PRES. This experiment aims to explore the impact of Panama Seaway closure on the ACC (Figures S6b and S7b in Supporting Information S1). We present the ocean current differences between the PRES and PLIO simulations to indicate the influence of Panama Seaway closure (Figures 7d and 7e).

There are three additional experiments with an open Panama Seaway to evaluate the impact of reduced Antarctic ice sheet volume and restricted DP width. Given that the general pCO_2 variability during the time span investigated (20–17.4 Ma and 14.6–5 Ma) was relatively small ($\sim$100–200 ppmv) (Rae et al., 2021) and that the presence and/or spatial extent of the West Antarctic Ice Sheet prior to and during the Pliocene is under debate (Kennett & Barker, 1990; Naish et al., 2009; Zachos et al., 2001), we use the PLIO conditions for the investigated time period and integrated for 1,000 years. Monthly output of the last 100 model years from each simulation was taken for analysis. The configuration for the reduced Antarctic ice sheet volume is in accordance with the Pliocene Model Intercomparison Project Phase 2 protocol (Figure S9 in Supporting Information S1) (Haywood et al., 2016). The simulated results with a retreated Antarctic ice sheet are displayed in Figures S6c and S7c in Supporting Information S1. The offsets in current velocity in response to the Antarctic ice sheet changes are displayed to show the impact of Antarctic ice volume (Figure 7c). For the preceding condition of a smaller
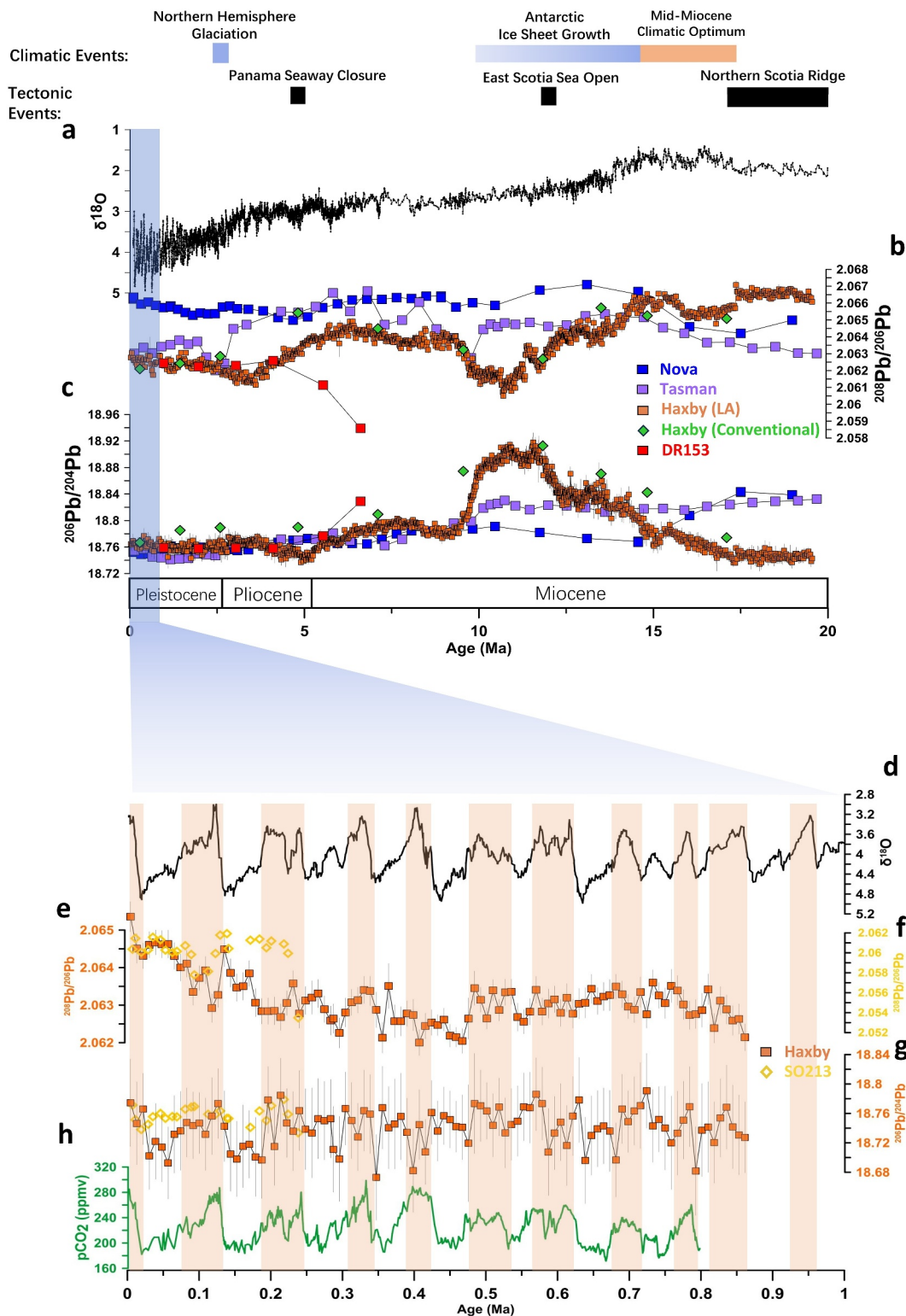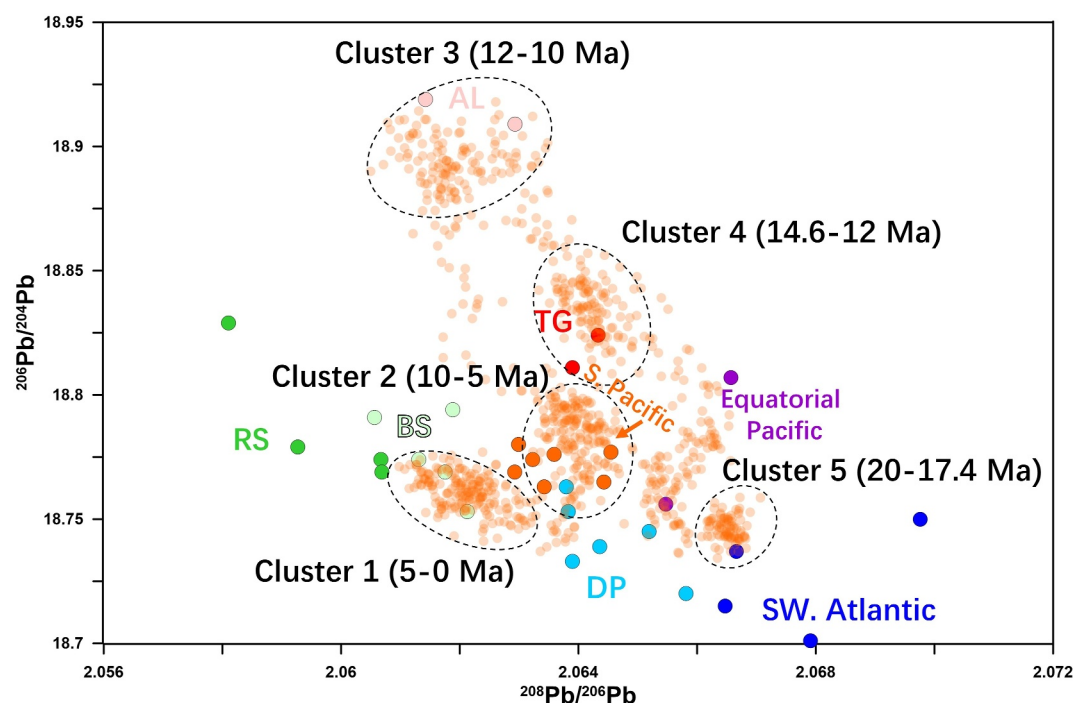
Figure 4.

Figure 5. Pb isotope variation in crust Haxby in $^{206}Pb/^{204}Pb$–$^{208}Pb/^{206}Pb$ spaces. The orange small dots indicate the seawater Pb isotope data recorded in ferromanganese crust Haxby. The larger colored dots mark the Pleistocene Pb isotopic signatures of ferromanganese nodules as shown in Figure 2 (Abouchami & Goldstein, 1995; von Blanckenburg et al., 1996). The five data clusters are denoted as Cluster 1 to 5 which are marked by dashed ellipses. RS: Ross Sea; AL: Adélie Land; TG: Tasman Gateway; DP: Drake Passage; BS: Bellingshausen Sea.

Antarctic ice sheet, we replaced ocean grids with land grids in DP in order to simulate the SO current changes as a function of the width of the DP (Figure S10 in Supporting Information S1). The width of the DP is configured to be 60% and 20% relative to that in PRES by replacing 4 and 8 ocean grids with land grids (Figures S6d–S6e and S7d–S7e in Supporting Information S1). The current velocity changes as a function of different widths of DP are presented in Figures 7a and 7b.

3. Results

The surface $^{10}Be/^9Be$ ratio of 0.7×10^{-7} in crust Haxby (Table S1 in Supporting Information S1) is very close to the surface $^{10}Be/^9Be$ ratios in surface scrapings of Fe-Mn nodules (0.9–1.3×10^{-7}) (Inoue et al., 1983) and crusts (0.8–1.2×10^{-7}) (van de Flierdt et al., 2004) in the Pacific Ocean. The growth rates calculated based on $^{10}Be/^9Be$ derived ages and Co-flux model are presented in Figure 3 and Table S4 in Supporting Information S1 following the same approach as in (van de Flierdt et al., 2004). The $^{10}Be/^9Be$ results define three different growth rates in the top 28.4 mm of the crust while no ^{10}Be was detectable below 28.5 mm depth. The topmost four $^{10}Be/^9Be$ data points and following three data points show nearly identical growth rates of 1.74 and 2.32 mm/Ma, respectively. The growth rate in the oldest section down to 28.4 mm depth in the crust was higher at 3.68 mm/Ma. Below

Figure 4. Compilation of global paleoclimatic events and Pb isotopic evolution recorded by ferromanganese crusts and marine sediments over the past 20 Ma. (a) and (d) Globally stacked benthic oxygen isotope record ($\delta^{18}O$) (Zachos et al., 2001); (b) $^{208}Pb/^{206}Pb$ time series of ferromanganese crusts Haxby, DR153 (Frank et al., 2002), Tasman (van de Flierdt et al., 2004) and Nova (van de Flierdt et al., 2004); (c) $^{206}Pb/^{204}Pb$ evolution of ferromanganese crusts Haxby (including 2 SD error bars), DR153 (Frank et al., 2002), Tasman (van de Flierdt et al., 2004) and Nova (van de Flierdt et al., 2004); (d) Benthic foraminiferal $\delta^{18}O$ stack for the last 1 Myr (Zachos et al., 2001); (e) $^{208}Pb/^{206}Pb$ evolution in crust Haxby (including 2 SD error bars); (f) $^{208}Pb/^{206}Pb$ ratios in sediment core SO213 (Molina-Kescher et al., 2016); (g) $^{206}Pb/^{204}Pb$ ratios in crust Haxby (including 2 SD error bars) and sediment core SO213 (Molina-Kescher et al., 2016); (h) Atmospheric CO_2 concentrations from the East Antarctic EPICA Dome C ice core (Lüthi et al., 2008). The timing of climatic and tectonic events is taken from previous studies (Barker, 2001; Dalziel et al., 2013; Haug & Tiedemann, 1998; Shevenell et al., 2004, 2008; Zachos et al., 2001). The orange boxes indicate warm/interglacial periods and white intervals indicate cold/glacial periods.

28.4 mm, the growth rates are only estimated via the Co-flux model. As shown in Figure 3, the Co-flux age model is calculated with an average value of the two sections with similar Co growth pattern constrained by tie points instead of using high-resolution records of 30 μm increments per data point. The higher growth rate of 3.68 mm/Ma between 28.4 and 35.3 mm is confirmed by Co-flux data. From 35.3 mm to the bottom of the sections, the growth rate was again lower at 2 mm/Ma. We would like to note that the samples for $^{10}Be/^9Be$ and Co-flux determination were sampled along separate tracks. Similar growth rates derived from these two methods demonstrate that the age model is robust. Supported by the $^{10}Be/^9Be$ dating results, the uncertainties for the younger (<10 Ma) Co-flux derived age is likely smaller than 1 Ma, while the age older than 10 Myr may have a larger uncertainty with a conservative error estimate of 2 Ma. Due to these uncertainties in dating, only general trends lasting longer than 1 million years will be discussed, with no attempt to determine the absolute timing of any transient event.

The long-term $^{206}Pb/^{204}Pb$ and $^{208}Pb/^{206}Pb$ records (analyzed by larger laser spot sizes) are generally consistent with the results obtained by the conventional approach (Figures 4b and 4c). The small offset for some sampled depths can be explained by the different sampling techniques. The laser ablation method only releases materials from the very surface of the sample while the conventional method needs to drill deep enough into the crust to acquire sufficient material for analyses, which might thus include sample material from different layers. The age uncertainty can also contribute to the offset especially for the oldest two data points analyzed by the conventional approach which has not undergone normalization of the Co-flux data. However, these age offsets are within our estimated uncertainty and do not affect our conclusions. The ages for the youngest part of our high-resolution Pb records (analyzed by smaller laser spots) are derived from the ferromanganese crust section dated by $^{10}Be/^9Be$, which still yields relatively large uncertainties for resolving precise ages of orbitally driven changes. Nevertheless, our high-resolution $^{206}Pb/^{204}Pb$ record for the past 250 kyrs largely co-vary with the records of authigenic Pb isotope compositions extracted from nearby sediment cores SO213-59-2 and SO213-60-1 (Molina-Kescher et al., 2016) (Figure 4g), atmospheric CO_2 concentration and deep-sea oxygen isotope records (Figures 4d and 4h). However, given the age uncertainties, whether those covariations are real awaits further verification and thus in this study we do not extend our discussions to orbital scale Pb isotope variations.

The long-term $^{206}Pb/^{204}Pb$ and $^{208}Pb/^{206}Pb$ records in crust Haxby are invariant from 20 to 17.4 Ma (Figures 4b and 4c). After 17.4 Ma, crust Haxby shows a $^{206}Pb/^{204}Pb$ increase from 18.74 to 18.92 and a $^{208}Pb/^{206}Pb$ decrease from 2.067 to 2.061 that lasts longer than seven million years. The long-term increase in $^{206}Pb/^{204}Pb$ and decrease in $^{208}Pb/^{206}Pb$ is terminated by a relatively abrupt and profound decrease in $^{206}Pb/^{204}Pb$ and increase in $^{208}Pb/^{206}Pb$ ratios at 10 Ma. Thereafter, throughout the past 10 Myr the $^{206}Pb/^{204}Pb$ ratio in crust Haxby only varied within a small range from about 18.80 to 18.74, whereas the $^{208}Pb/^{206}Pb$ variation between 2.065 and 2.061 is more pronounced.

Results only based on one Pb isotope ratio can be misleading. For example, the $^{206}Pb/^{204}Pb$ data of crust Haxby over the past 10 Myr are almost identical within error to the $^{206}Pb/^{204}Pb$ composition in ferromanganese crust Nova (water depth: 7,129 m) from the deep equatorial Pacific and ferromanganese crust Tasman from an intermediate water depth of 1,700 m in the SW Pacific Ocean (van de Flierdt et al., 2004), while the coeval $^{208}Pb/^{206}Pb$ ratios in these three crusts are very different (Figures 4b and 4c). In order to clearly resolve the differences of the Pb isotope signals at various sites and trends over time, we combine the $^{206}Pb/^{204}Pb$ and $^{208}Pb/^{206}Pb$ data and examine the Pb isotope variation in $^{206}Pb/^{204}Pb–^{208}Pb/^{206}Pb$ space (Figure 5). The Pb isotope signal of crust Haxby in $^{206}Pb/^{204}Pb–^{208}Pb/^{206}Pb$ space remained relatively stable within individual data clusters for millions of years followed by abrupt shifts to other distinct clusters (Figure 5). Five discernible data clusters can be identified in our 20 Myr record, which are denoted as Cluster 5 (20-17.4 Ma), Cluster 4 (14.6-12 Ma), Cluster 3 (12-10 Ma), Cluster 2 (10-5 Ma) and Cluster 1 (5-0 Ma) from oldest to youngest.

4. Discussion

4.1. Reconstruction of Seawater Pb Isotope Compositions

Recent surveys in the Pacific Ocean reveal that sinking particles throughout the water column can transport Pb from the upper water column to the abyssal ocean without significant water mass mixing (Lanning et al., 2023; Wu et al., 2010). However, evidence suggests that variations in Pb isotope signals in the deep water are primarily driven by changes in deep water dynamics and mixing. Despite substantial anthropogenic Pb input to the surface ocean, the seawater $^{207}Pb/^{206}Pb$ gradient remains distinct between deep and shallower waters in the North Pacific
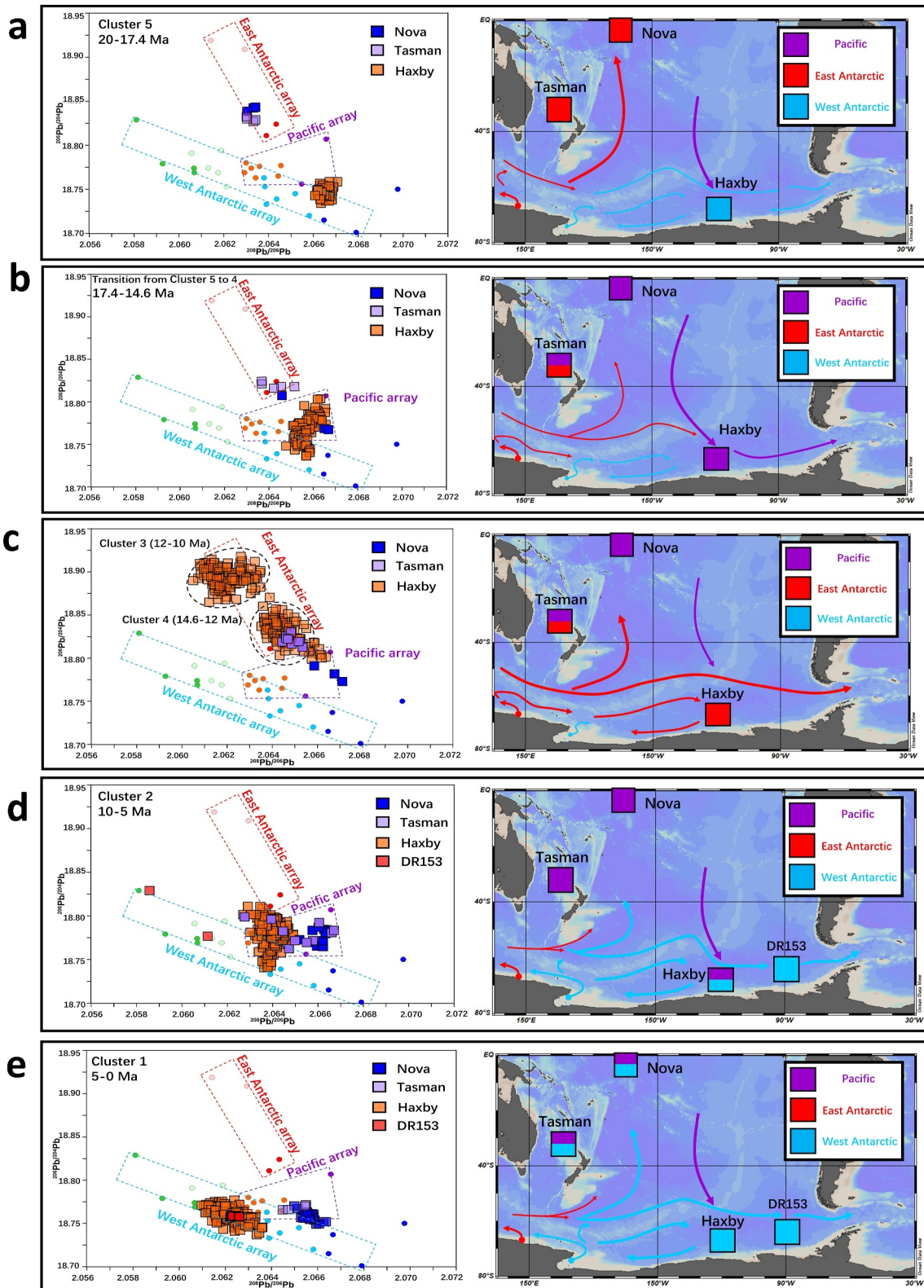
Figure 6.

(Wu et al., 2010), indicating that the surface Pb input could shift but could not fully homogenize the water column Pb isotope signal. The Pleistocene Pb isotope signal in crust Haxby and sediment core SO213-60-1 further support a dominant deep water pattern (Figure 2). Site SO213-60-1, bathed in LCDW that is supplied by AABW derived from RS, shows Pleistocene Pb isotope signals that align with the RS endmember, despite being influenced by overlying deep and shallow waters from the Pacific Ocean. Crust Haxby, situated at a shallower depth and closer to Antarctica compared to abyssal ferromanganese nodules (BS and RS in Figure 2), is more influenced by the Antarctic surface water. However, its Pleistocene Pb isotope signals are shifted closer to the Pacific Pb array, due to its proximity to PDW upwelling in the SO, indicating a deep water dominance. Moreover, the Pleistocene Pb isotope signal in crust Haxby is even more shifted toward the Pacific Pb array compared to sediment core SO213-60-1, despite its proximity to Antarctica. These observations suggest that deep water Pb isotope signals are largely determined by mixing of the deep water masses at each site. In the Pacific sector of the SO, the position of the UCDW/LCDW boundary is closely linked to the positions of the SO fronts and ACC, and the UCDW is primarily supplied by PDW. Therefore, it is reasonable to infer latitudinal shifts of the ACC through changes of PDW proportions relative to AABW signatures in crust Haxby.

A study of ferromanganese crusts from the central North Pacific suggests that overwhelming local inputs could have overprinted the ambient Pb isotope signal transported by advection (Chen et al., 2013). In the Amundsen Sea, the temporally variable dust input in the Pacific sector of the SO (Klemm et al., 2007; Struve et al., 2020) and/or incongruent chemical weathering of Antarctic basement rocks (Basak & Martin, 2013) could also potentially overprint water mass mixing signals. However, we consider the influence of these two factors insignificant for the following reasons: incongruent chemical weathering of fresh silicate material generated during ice sheet expansion may produce a more radiogenic Pb isotope signal (i.e., higher in $^{206}Pb/^{204}Pb$) than the parent source rocks (Basak & Martin, 2013; Crocket et al., 2012; Dausmann et al., 2019; Gutjahr et al., 2009; Kurzweil et al., 2010) due to preferential release of radiogenic Pb from accessory minerals and/or sites of radiation damage (Erel et al., 2004). The Antarctic ice sheet extensively expanded between ~15 Ma and 12 Ma (Hochmuth et al., 2020; Miller et al., 2020; Shevenell et al., 2004, 2008), but the $^{206}Pb/^{204}Pb$ ratio in crust Haxby remained nearly unchanged from 14 to 12 Ma (Figure 3c). Additionally, the marked decline of $^{206}Pb/^{204}Pb$ at 10 Ma did not coincide with any known events for significant Antarctic ice sheet changes. Although the available data do not allow us to fully isolate the influence of incongruent chemical weathering on our Pb isotope record in detail, the lack of covariation between $^{206}Pb/^{204}Pb$ ratios and contemporaneous Antarctic ice-sheet dynamics makes incongruent chemical weathering as a dominant control an unlikely explanation for the observed Pb isotope variations.

The potential for direct dust deposition on Haxby Seamount is minimal due to two factors: (a) Antarctica is characterized by exceptionally low dust fluxes, making it one of the least dust-affected regions globally (Mahowald et al., 2011); and (b) Haxby Seamount, where the ferromanganese crust formed, experiences high current speeds and minimal sedimentation, further reducing the likelihood of significant dust accumulation. This is corroborated by the observation that today the geochemical provenance fingerprint of fine-grained detritus in deep sea surface sediments near the Marie Byrd Seamounts is predominantly of Antarctic origin (Simões Pereira et al., 2018) and does not reflect the notable dust signal in sediments close to the APF and further north (Wengler et al., 2019). Even though dust deposition in the Pacific sector of the SO was likely three times higher during glacial periods than during interglacials (Lamy et al., 2014), the provenance of glacial sediments deposited all along the Pacific margin of Antarctica has still been dominated by continental sources in the West Antarctic hinterland (Farmer et al., 2006; Hillenbrand et al., 2009, 2021). Furthermore, Haxby Seamount is situated just north of the average summer sea-ice limit and well south of the winter sea-ice limit during the present interglacial (e.g., Hillenbrand et al., 2009), and thus was likely under perennial sea-ice cover during past glacial periods (e.g. (Bostock et al., 2013)), which would have shielded crust Haxby from dust deposition. Besides, the dust particles

Figure 6. Temporal and spatial Pb isotope variability in different time slides over the past 20 Myr. (a) Time span of 20–17.4 Ma; (b) Time span of 17.4–14.6 Ma; (c) Time span of 14.6–10 Ma; (d) Time span of 10–5 Ma; (e) Time span of 5–0 Ma. Diagrams on the left side show the $^{206}Pb/^{204}Pb$–$^{208}Pb/^{206}Pb$ distributions of the four ferromanganese crusts (filled squares) compared with different endmembers through time. The dashed retangles with different colors indicate the East Antarctic, West Antarctic and Pacific arrays and the colored dots indicate the Pleistocene Pb isotopic signatures of ferromanganese nodule as shown in Figure 2. The illustrations in the right column represent the approximate fractional source contributions of seawater Pb recorded in four ferromanganese crusts. Purple, red, and blue colors indicate Pb supplied from the South Pacific, East Antarctica, and West Antarctica, respectively. The colored rectangles reflect the approximate fractions of various sourced Pb in the individual crust, and the colored arrows suggest the inferred deep circulation that transported different sourced Pb.
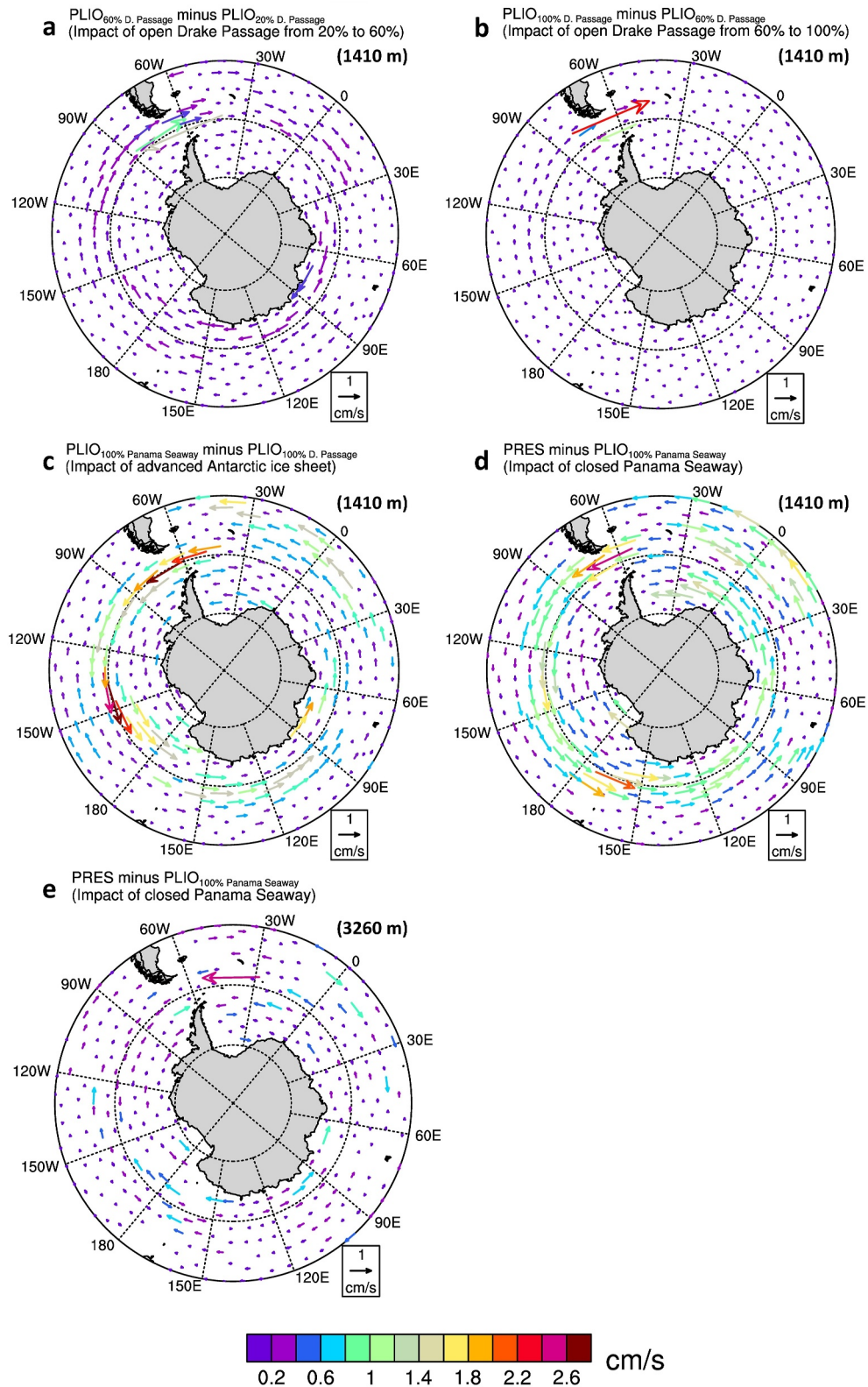
Figure 7.

may also have gradually released Pb into ambient seawater when settling through the water column and/or during deposition, thereby changing the dissolved seawater Pb isotope signature when the dust sourcing changed. For example, the South Pacific Subantarctic Zone was dominated by dust from Central South America with a highly radiogenic Pb isotopic signal ($^{206}Pb/^{204}Pb > 19$) during the last glacial period, whereas the modern/Holocene pattern is thought to be primarily supplied by less radiogenic Australian sources ($^{206}Pb/^{204}Pb < 19$) (Struve et al., 2020). However, the authigenic Pb isotope signals extracted from two sediment cores recovered in the deep South Pacific (SO213-59-2 and SO213-60-1 in Figure 1) (Molina-Kescher et al., 2016) show more radiogenic Pb isotope compositions in Holocene than in last glacial sediments (Figure 4g), which is opposite to the trend of dust Pb isotopic variations recorded in the same cores, documenting that the seawater Pb isotope signature has not been a function of dust source variations.

In this study, we find limited data on significant long-term variability of Pb endmembers. Comparing our Pb isotope records with those from ferromanganese crust Nova, ferromanganese crust Tasman (van de Flierdt et al., 2004) and ferromanganese crust DR153 (water depth: 3,150–3,300 m) from the DeGerlache Seamounts in the BS (Frank et al., 2002), we observe consistent results within a three-endmember Pb mixing array, defined by RSBW, ALBW, and Pacific deep waters, over the past 20 Myr (Figures 6a–6e).

4.2. Weak ACC Flow in the Early Miocene (20-17.4 Ma)

In the early Miocene, crusts Nova and Tasman show almost identical Pb isotope signals falling into the East Antarctic Pb array (Figure 6a), which is attributed to efficient northward export of deep and bottom waters from the SO to the equatorial Pacific (van de Flierdt et al., 2004). The data show that the export of SO water masses was likely continuously active during this time period, consistent with benthic foraminiferal carbon isotope ($\delta^{13}C$) data indicating that the deep South Pacific was persistently supplied by SO bottom waters since 23 Ma (Woodruff & Savin, 1989). Interestingly, East Antarctic Pb isotope signals as recorded in crusts Nova (~1°S) and Tasman (~28°S) could not be delivered to the deep South Pacific north of ~50° S by AABW during the Pleistocene (Figures 6a and 6e), implying a much stronger northward export of SO deep and bottom waters during the early Miocene. The strong northward export of these waters to the locations of crusts Nova and Tasman may have been caused by the clockwise proto-Ross-Gyre that deflected the circumpolar waters at the northern edge of the Tasman Sea. However, this effect is unlikely the primary cause because it was largely diminished after the Oligocene (Pfuhl & McCave, 2005). Alternatively, the strong northward export of SO deep and bottom waters may also have been a result of the enhanced production of deep water derived from the AL margin because the Pb isotope signatures of crusts Nova and Tasman resemble the East Antarctic Pb signal originating from AL. Modern ALBW has a less radiogenic Nd isotope signature (εNd of −8.9) (Lambelet et al., 2018) than RSBW (εNd of −6.6) (Rickli et al., 2014). The strong northward export of deep water sourced from the AL region is also supported by the less radiogenic Nd isotope signals than today recorded in crust Nova from 20 to 17.4 Ma (van de Flierdt et al., 2004). However, the less radiogenic Nd is not notable in a recent Nd isotope record at DSDP Site 278 from Southwest Pacific (Evangelinos et al., 2024).

During this time, the Pb isotope signal of Cluster 5 in crust Haxby differs from that in the SW Pacific but closely matches the West Antarctic array, similar to the surfaces of more easterly ferromanganese nodules in the DP and SW Atlantic (Abouchami & Goldstein, 1995). Identification of Cluster 5 signals in the Amundsen Sea during the

Figure 7. Modeled responses of Southern Ocean circulation at different water depth to different tectonic and Antarctic ice volume changes. Both the length and color of the vectors in each map represent the current velocity offsets between different model scenarios with magnitudes indicated by the color shading at the bottom. A current velocity change of 1 cm/s for a given configuration is also indicated by the length of the arrow in the box at the bottom right. The arrow of the vectors indicates the direction of the current velocity offset. The gray shading in all figure panels indicates the modern continental areas above sea level. (a) current changes at 1,410 m water depth between a 60% open Drake Passage (DP) and a 20% open DP; (b) Current changes at 1,410 m depth between a fully open and a 60% open DP; (c) Current differences at 1,410 m depth as a result of increased or decreased Antarctic ice volume; (d) Current differences at 1,410 m depth between a closed and fully opened Panama Seaway; (e) Current differences at 3,260 m depth between a closed and fully open Panama Seaway. The modeling results suggest that a DP opening by 20%–60% (in respect to today) enhances Antarctic Circumpolar Current (ACC) current strength between 50 and 60°S in the Pacific sector as well as eastward directed current flow along the East Antarctic margin, while DP widening from 60% to 100% has only a negligible impact on ACC vigor, corroborating that the major hydrographic changes took place during the early widening of DP. A more expanded and thicker Antarctic ice sheet weakens the ACC in the SO's Pacific sector at about 60°S latitude, while simultaneously strengthening deep water export from the Ross Sea (RS) to the east and current flow along the West Antarctic continental margin. The final closure of the Panama Seaway resulted in partially opposite current changes at different water depths. The eastward deep water export from the RS increases at 1,410 m water depth but decreases at 3,260 m depth.

early Miocene (20-17.4 Ma) suggests either a weak ACC unable to deliver Pb further to the east, and/or a westward flow of recirculated deep waters along the West Antarctic margin to the Marie Byrd Seamounts from further east that might have been caused, for example, by reduced eastward ACC flow through a more restricted and/or shallower DP (Barker, 2001). Evidence for a weaker early Miocene ACC compared to today is supported by sortable silt data from the Southwest Pacific (Evangelinos et al., 2024).

The DP was narrower in the early Miocene than today and subsequently expanded to its modern width by the late Miocene (Barker, 2001; van de Lagemaat et al., 2021). We tested the effect of changes in ACC velocity and latitudinal position using the KCM. Figure 7a shows the current changes at 1,410 m water depth when allowing ACC water to flow through a DP with 60% and 20% of today's width. Our simulations indicate that a more restricted DP results in a stronger westward flowing current from the DP to the Amundsen Sea along the West Antarctic margin (Figure S6e in Supporting Information S1). A reduction of the DP width from 60% to 20% also leads to a ~0.4 cm/s slower (~20% slower) ACC near 60°S in the Pacific sector (Figure 7a), which is generally consistent with our proxy results. Besides, the weak ACC could also be caused by a limited throughflow of the ACC across the Tasmanian Gateway in response to a more restricted Australian palaeobathymetry (Evangelinos et al., 2024).

4.3. Dominance of Pacific Deep Water (17.4-14.6 Ma)

Between 17.4 and 14.6 Ma, Pacific Pb isotope signals were dominant at the locations of both crust Nova and crust Haxby, and the signatures of crust Tasman also shifted toward the Pacific Pb array (Figure 6b). Given that the deep SO in the Pacific sector was likely constantly occupied by AABW at that time (Woodruff & Savin, 1989), the Pacific-sourced Pb was most likely delivered via PDW into UCDW in the shallower part of the water column. The modern UCDW/LCDW boundary in the Pacific sector of the SO at the water depth of crust Haxby (~1,500–1,700 m) is located at about 60°S (Talley, 2013). The dominating equatorial Pacific Pb isotope signature in crust Haxby (~69°S) at the time thus required a southward shift of the UCDW/LCDW boundary by at least 9° latitude facilitated by a southward shift of the ACC, if the SO water column structure was comparable to today. The dominance of Pacific Pb isotope signatures in the records of crusts Nova and Tasman is also consistent with a previously inferred strengthening of the regional circulation in the deep and intermediate Pacific (van de Flierdt et al., 2004).

Interestingly, in $^{206}Pb/^{204}Pb$–$^{208}Pb/^{206}Pb$ space the Pb isotope signal of crust Haxby was gradually moving from Cluster 5 to 4 rather than varying within a confined cluster between 17.4 and 14.6 Ma. In particular, the Pb isotope change is marked by an initial relatively abrupt decrease in $^{208}Pb/^{206}Pb$ at 17.4 Ma followed by a gradual increase in the $^{206}Pb/^{204}Pb$ ratios until about 14.6 Ma (Figures 4b and 4c). The abrupt decrease of $^{208}Pb/^{206}Pb$ shifts the Cluster 5 to match the Pb isotope signal in the more westerly located ferromanganese nodules in the West Antarctic array (Figures 2 and 5). As discussed in Section 4.2, this change likely suggests either a strengthened ACC that was able to deliver Pb further to the east, and/or advection of less recirculated deep waters that were redirected by bathymetric barriers in the deep DP. The deep opening of DP has been proposed to have caused an abrupt enhancement of ACC strength and change of ACC flow path in the Oligocene, deflecting the flow of CDW from a northerly to an eastward direction at the exit of TG (Pfuhl & McCave, 2005). The abrupt ACC enhancement at 17.4 Ma may have been caused by a similar mechanism given that it corresponded to the opening of the North Scotia Ridge in DP (22-17 Ma) (Barker, 2001), which established a deeper gateway toward the Atlantic sector of the SO. The following progressive Pb isotopic evolution in crust Haxby toward equatorial Pacific dominated signatures supports a strengthening of deep Pacific circulation previously attributed to the stepwise closure of the Indonesian Seaway (van de Flierdt et al., 2004). Thus, the Pb isotope change between 17.4 and 14.6 Ma is likely a result of the competitive effect of progressive Indonesian Seaway closure and North Scotia Ridge opening, while the enhanced poleward export of PDW in response to Indonesian Seaway closure was gradually becoming dominant.

4.4. Increased Bottom Water Origin From Adélie Land (14.6-10 Ma)

Clusters 4 and 3 (14.6-10 Ma) represent the most profound Pb isotope changes in crust Haxby when Pb derived from East Antarctic sources dominated the water column in the Amundsen Sea (Figure 6c). Inferred from the predominant ALBW in the deep SO offshore from AL today, this East Antarctic Pb isotope signal suggests a high proportion of ALBW in the SO basins in the Pacific sector that was entrained into LCDW and subsequently

upwelled to Marie Byrd Seamounts. In contrast to Cluster 4 (14.6-12 Ma), the younger Cluster 3 (12-10 Ma) Pb isotope signature of crust Haxby was even more radiogenic and hence consistent with Pb isotope compositions of surface scrapings from ferromanganese nodules on the AL margin. It is worth noting that the East Antarctic sourced Pb is also recorded in crust Tasman and remained almost unchanged during 14.6-10 Ma (Figure 6c), which suggests that the Pb isotope signature of ALBW was not significantly different from today during this time. If this is correct, the more radiogenic Pb isotope signals of Cluster 3 (12-10 Ma) strongly suggest a higher proportion of ALBW in the deep Amundsen Sea.

Importantly, East Antarctic Pb sourced from AL cannot reach the Amundsen Sea in the modern SO because eastward transport of ALBW is blocked by RSBW that flows northward within the Ross Gyre. Between 150°E and 160°W, that is, at the same longitude where the present-day ALBW Nd signature (εNd = −8.9) (Lambelet et al., 2018) changes to a RSBW Nd isotope signature (εNd = −6.6) (Basak et al., 2015; Rickli et al., 2014), the $^{206}Pb/^{204}Pb$ ratios in nodule surfaces also decrease abruptly from a maximum value of ~18.92 offshore AL to an intermediate value of ~18.8 in the RS (Abouchami & Goldstein, 1995), with all nodules further to the east being dominated by a West Antarctic Pb isotope signature (Figure 2). Correspondingly, the modern observations show almost no ALBW component in the deep Amundsen Sea (Solodoch et al., 2022). The East Antarctic Pb isotope signatures recorded in crust Haxby thus suggests contributions or even dominance of ALBW to AABW from 14.6 to 10 Ma to the north of the Amundsen Sea, which disappeared at around 10 Ma. Sea ice formation in polynyas is an essential precondition for the production of precursor water masses of modern AABW. At several locations around Antarctica, cold and dense shelf waters are produced by brine rejection during sea-ice formation in polynyas in front of ice shelves. The dense shelf waters then flow down the continental slope and mix with overlying water masses to form AABW (Purkey et al., 2018). Palynological and dinocyst evidence suggests sea ice was present after the Mid-Miocene Climatic Optimum (MMCO) at IODP Site U1356 offshore Wilkes Land (Bijl et al., 2018; Sangiorgi et al., 2018), where ALBW forms today. We thus attribute the powerful ALBW production to be the result of enhanced regional sea ice formation offshore AL.

It is also worth considering the possibility that the observation of a significant East Antarctic Pb isotope signal in the Amundsen Sea from 14.6 to 10 Ma was influenced by a change of the RSBW Pb endmember. Extensive Antarctic ice sheet growth during the middle Miocene caused significant changes in sediment deposition rate and sediment provenance (Hochmuth et al., 2020). The outlet glaciers terminating in the western RS that eroded East Antarctic terrains during the middle Miocene Antarctic ice sheet expansion (Levy et al., 2016; Pérez et al., 2022) may have delivered substantial quantities of Pb from East Antarctic terrains to the RS and may have labeled RSBW with an East Antarctic Pb isotope signature. The detailed influence of a potential endmember change is difficult to assess based on the currently available Pb isotope records, but some evidence suggests that the change in sediment sourcing was not the major factor driving the seawater Pb isotope signature. First, a change in the RSBW signature should have led to an overall shift in the AABW Pb isotope signal, but an increased ALBW signal during the time interval from 12 to 10 Ma was only recorded by crust Haxby, not by crust Tasman, while they were both bathed by AABW (Figure 6c). Although a major increase in sedimentation rate around Antarctica from ~14 to 12 Ma (Hochmuth et al., 2020) coincided with the duration of the Cluster 4 signature in crust Haxby, the younger Cluster 3 (12-10 Ma) with a mostly East Antarctic dominated Pb isotope signal in crust Haxby occurred alongside reduced sedimentation rates around both East and West Antarctica (Hochmuth et al., 2020). In addition, the terrigenous Nd isotope record for IODP Site U1521 in the central RS documented a sediment provenance change at ~17.72-17.40 Ma in response to a major West Antarctic Ice Sheet expansion (Marschalek et al., 2021), while no corresponding seawater Pb isotope change was recorded in either crust Haxby or crust Tasman.

Compared with the transition period prior to the recording of Cluster 4 and 3 in crust Haxby (17.4-14.6 Ma), the diminished Pacific Pb isotope signal recorded from 14.6 to 10 Ma points to reduced southward export of PDW and a northward ACC extension. This finding is in agreement with a coeval increase of the $\delta^{13}C$ gradient between deep and intermediate water masses in the south Pacific (Holbourn et al., 2013), which has been interpreted as a result of a more isolated PDW (Ma et al., 2018). The northward shift of the ACC may have been a result of declining atmospheric pCO_2 resulting in advances of the Antarctic ice sheet, expansion of sea ice, and a northward shift of both the westerlies and the main SO fronts (DeConto et al., 2008; Sangiorgi et al., 2018). The overall sensitivity to atmospheric CO_2 forcing seems to have been lower for Miocene Antarctic ice sheets than for their late Pleistocene counterparts. For instance, reconstructed Miocene atmospheric pCO_2 variations are about twice as large as late Pleistocene variations (300–500 ppmv compared to 180 to 280 ppmv), but the amplitude of the

changes of benthic $\delta^{18}O$ and sea level in the Miocene was smaller than in the late Pleistocene (Foster & Rohling, 2013; Greenop et al., 2014). Reconstructed atmospheric pCO$_2$ declined by approximately 100 ppmv over the Middle Miocene Climate Transition (MMCT) at ~14 Ma (Foster et al., 2012; Zhang et al., 2013; Consortium et al., 2023). However, a similar magnitude of pCO$_2$ decline during late Pleistocene glacial cycles (Lüthi et al., 2008), when CO$_2$ forcing of Antarctic ice sheet growth was stronger, was not sufficient to cause Pb isotopic change between Pb isotope clusters (Figure 6e). Moreover, major pCO$_2$ fluctuations between high values over 500 ppmv and low values below 300 ppmv, and large-scale ice volume changes occurred multiple times from ~17 to 14 Ma (Greenop et al., 2014; Levy et al., 2016). If indeed the 100 ppmv decline of pCO$_2$ at ~14 Ma was capable of causing the circulation change recorded by Pb isotope Cluster 4, then the larger scale pCO$_2$ decline from ~17 to 14 Ma should have caused ocean circulation changes of similar or even larger magnitude multiple times. However, the shift into Pb isotope Cluster 4 was clearly only a single event lasting about 1 million years at around 14.6 Ma.

Given the lack of obvious atmospheric drivers, we thus suspect that tectonic processes have played the main role in the circulation change recorded at 14.6 Ma. One possible cause is the closure of the Indonesian seaway during the early Middle Miocene (17-15 Ma) (Nishimura & Suparka, 1997) that intensified Pacific gyre circulation (Kennett, 1985). One piece of evidence supporting this scenario is that the gradual increase of the ^{206}Pb/^{204}Pb ratio in crust Haxby from ~17 to 14.6 Ma coincided with the decline of the ^{206}Pb/^{204}Pb ratio in crust Nova (Figure 4c), which occurred in response to the strengthening of Pacific deep circulation (van de Flierdt et al., 2004). In addition, the onset of gradual increase in ^{206}Pb/^{204}Pb signatures from ~17 to 14.6 Ma also followed the North Scotia Ridge opening at ~17.5 Ma and the gradual latitudinal extension of the DP that persisted until the late Miocene (Barker, 2001; van de Lagemaat et al., 2021). As shown in Figure 6a, the widening of DP from 20% to 60% of its modern width can lead to an about 20% higher current speed at 1,410 m water depth near 60°S in the Pacific sector of the SO, but further DP opening from 60% to 100% width then only had a subtle effect on ACC strength (Figure 7b). If the long-term opening of DP reached a critical width at ~14.6 Ma, it is possible that it also caused at least part of the circulation change recorded by the Pb isotope Cluster 4 (14.6–12 Ma). We thus suspect that Pb isotope Cluster 4 resulted from combined tectonic changes related to Indonesian Seaway closing and DP widening. Future proxy and modeling studies are required to better constrain the mechanism that caused ACC strengthening at ~14.6 Ma.

4.5. Dominance of RSBW (10-5 Ma)

Between 10 and 5 Ma, deep water circulation in the SO's Pacific sector already resembled the modern pattern. No significant East Antarctic Pb isotope signal was recorded in any of the four analyzed crusts during this period (Figure 6d). This finding indicates that, similar to today (Purkey et al., 2018; Solodoch et al., 2022), ALBW was no longer the dominant AABW variety in the Pacific sector. On the other hand, the now clearly resolvable West Antarctic Pb isotope signal in the Amundsen and Bellingshausen seas during this time interval (Frank et al., 2002) documents enhanced RSBW production. Compared with the middle Miocene (17.5-14.6 Ma), the Pb isotope composition of crust Haxby during this period contained less of a Pacific component (Figures 6b and 6d), indicating a northward shift of the ACC. However, the ACC was likely located not as far North as during the Pleistocene because the Pacific Pb signal still was a more prominent component in crust Haxby from 10 to 5 Ma than during the Pleistocene (Figures 6d and 6e). The DP had already attained its full width at 10 Ma (van de Lagemaat et al., 2021), and thus cannot have caused the drastic circulation change at that time. Instead, the continued growth of the Antarctic ice sheet may have shifted the ACC position through a complex interplay between wind field, ocean circulation and the sea-ice system (Knorr & Lohmann, 2014). The increase in RSBW export at ~10 Ma coincided with enhanced middle Miocene Antarctic ice sheet growth (Flower & Kennett, 1995; Vincent et al., 1985; Zachos et al., 2001). As shown in Figure 6c, our simulations indicate that the thicker and more expanded Antarctic ice sheet led to enhanced eastward deep water flow from the RS into the Amundsen Sea, and a more vigorous clockwise current circulation along the Pacific margin of West Antarctica, likely driven by wind field changes induced by ice sheet expansion.

4.6. Modern ACC Configuration (5-0 Ma)

Around 5 Ma, the Pb isotope signals in crusts DR153 and Haxby finally converged to their homogeneous Pleistocene signatures, despite the difference in water depths between the two crusts (Figure 6e). Specifically, the shallower crust Haxby showed an increased influence of a West Antarctic Pb isotope signal, while the deeper

crust DR153 exhibited a less prominent RS Pb isotope signature. This change can be attributed to the reduced presence of RSBW at depth and enhanced export of Pb sourced from the RS into the Amundsen Sea at shallower water depths. Alternatively, the elimination of the Pb isotope gradient in the deep and abyssal SO from the Pacific sector may also indicate stronger vertical mixing driven by more vigorous ACC dynamics. Another possibility is that the eastern limb of the Ross Gyre extended far enough to influence crust DR153 prior to 5 Ma and then shifted westward after 5 Ma, leading to the reduced RS Pb isotope signal recorded in crust DR153. Currently, crust Haxby is situated under the easternmost limb of the Ross Gyre, while crust DR153 is located outside the Ross Gyre (Wåhlin et al., 2013).

These circulation changes coincided with the final stage of the closure of the Panama Seaway at 4.6 Ma (Burton et al., 1997; Haug & Tiedemann, 1998), which prevented low-salinity waters from the equatorial Pacific to enter the Atlantic at mid-latitudes, likely resulting in an overall stronger Atlantic Meridional Overturning Circulation (AMOC) (Zhang et al., 2012). Originating in the North Atlantic, where cold, salty water sinks to form North Atlantic Deep Water (NADW), the AMOC plays a key role in supplying deep water to the modern circumpolar circulation system (Talley, 2013). The earliest estimate for NADW initiation is proposed at ∼50 Ma, coinciding with the inception of the Cenozoic global cooling trend (Hohbein et al., 2012). However, another body of studies suggests that the initiation of NADW was closely associated with the onset of large-scale Antarctic glaciation at the Eocene/Oligocene transition, 34.44-33.65 Ma (Abelson & Erez, 2017; Coxall et al., 2018; Wang et al., 2023). Regardless of its precise timing, the AMOC structure remained in a prototype state until the Miocene. The Nd isotope and benthic foraminiferal δ^{13}C records suggest that the modern-like AMOC geometry began to develop around 10-9 Ma due to a major step in the closure of the Isthmus of Panama and the consequent cessation of low-salinity Pacific waters entering the Caribbean (Kirillova et al., 2019; Woodruff & Savin, 1989). This timing aligns with the onset of modern-like ACC in the Pacific sector of the SO as indicated by our Pb data at ∼10 Ma (Section 4.5). This coincidence suggests that the simultaneous intensification of NADW and RSBW production was instrumental in shaping the modern-like ACC structure. Benthic foraminiferal δ^{13}C records and model simulations suggest that the final closure of the Panama Seaway at ∼5 Ma had further enhanced the AMOC (Fyke et al., 2015; Karas et al., 2017), which is also supported by our model results (Figures S8a and S8b in Supporting Information S1). This change occurred along with a reduced presence of RSBW at depth (3,260 m) and enhanced export of RS waters into the Amundsen Sea at shallower water depths, similar as indicated by Pb isotope record (Figure 7e). The combined development of RSBW and an enhanced AMOC contributed to the formation of the modern ACC system, making variability in the Ross Gyre a less likely explanation. Our findings reveal a close connection between the ACC and AMOC since the middle Miocene, suggesting that a strong AMOC state was critical for fully establishing the modern ACC system. Based on the Pb isotope time series, the Pleistocene ACC configuration was likely established by ∼5 Ma.

No substantial further changes in seawater Pb isotopic composition were observed in any of the crusts apart from the change in the crust Tasman at ∼3 Ma, caused by an imprint of Pb originating from local volcanic sources (van de Flierdt et al., 2004). Remarkably, the onset of Northern Hemisphere glaciation (Raymo et al., 1992; Ruddiman et al., 2017; Shackleton & Opdyke, 1977) and closure of the restricted Indonesian Seaway (Karas et al., 2011) at 3.5–3 Ma were suggested to have caused a fundamentally altered deep ocean circulation, but the minor and hardly resolvable Pb isotopic differences during this time interval in all crusts studied here argue against such a pronounced circulation change. Compared with the earlier oceanographic changes discussed above, the intensification of Northern Hemisphere glaciation hence apparently only had very limited impact on ACC flow in the Pacific sector of the SO.

Another important detail is that the ^{206}Pb/^{204}Pb record in crust Haxby shows significant orbitally driven variations over the past 850 kyrs, but the ^{206}Pb/^{204}Pb–^{208}Pb/^{206}Pb ratios only fluctuate within Cluster 1 (Figure 6e). Therefore, the mechanism shifting the Pb isotope compositions from one cluster to another was unlikely of orbital origin.

5. Conclusions

Our long-term seawater Pb isotope records of the past 20 Myr resolve five relatively stable and million-year long circulation states of the ACC. According to our new data, the long-term evolution of ocean circulation in the South Pacific and the SO's Pacific sector was characterized by several clearly defined step changes during discrete events rather than gradual changes.

Earth's final transition into the present "icehouse" state occurred after the MMCT at about 14 Ma (Holbourn et al., 2005) and was accompanied by major ice-sheet expansion on the Antarctic continent (Gulick et al., 2017; Zachos et al., 2001). Large-scale reorganizations of ocean circulation have long been suggested to have promoted ice sheet expansion in Antarctica by preventing poleward heat transport from low latitudes (Kennett, 1977). Our results show that the southward shift of the ACC and enhanced poleward export of PDW between 17.4 and 14.6 Ma coincided with the warm MMCO and substantial Antarctic ice sheet melting (Levy et al., 2016; Shevenell et al., 2008). The following MMCT was marked by ∼2°C cooler temperatures in the SO (Shevenell et al., 2004) and Antarctic ice sheet expansion (Holbourn et al., 2005), and coincided with a significant circulation change in the Pacific sector of the SO involving the enhanced export of ALBW and a northward shift of the ACC. We mainly attribute these circulation changes to tectonic processes, possibly also superimposed by climatic effects associated to the decline of atmospheric pCO$_2$.

We find that a circulation regime close to the modern ACC in the study area formed after about 5 Ma, probably as a consequence of the closure of the Panama Seaway. The onset of a modern type ACC circulation occurred long after the opening of the two main SO gateways, that is, the TG and DP. This is in agreement with modeling results, which suggest that the simple opening of these two SO gateways is not sufficient to generate the modern ACC flow (Evangelinos et al., 2024; Sauermilch et al., 2021). Overall, the results of our study offer novel insights into distinct Neogene circulation changes in the SO with important implications for the understanding of the interaction between ACC evolution, tectonic activity and Antarctic ice sheet changes.

Data Availability Statement

Ferromanganese crust PS75/247-2 is stored at GEOMAR Helmholtz Centre for Ocean Research Kiel, Germany. All new data presented in this manuscript are available online in the PANGAEA data repository (Huang et al., 2024).

References

Abelson, M., & Erez, J. (2017). The onset of modern-like Atlantic meridional overturning circulation at the Eocene-Oligocene transition: Evidence, causes, and possible implications for global cooling. *Geochemistry, Geophysics, Geosystems*, *18*(6), 2177–2199. https://doi.org/10.1002/2017GC006826

Abouchami, W., & Goldstein, S. L. (1995). A lead isotopic study of circum-antarctic manganese nodules. *Geochimica et Cosmochimica Acta*, *59*(9), 1809–1820. https://doi.org/10.1016/0016-7037(95)00084-D

Barker, P. F. (2001). Scotia Sea regional tectonic evolution: Implications for mantle flow and palaeocirculation. *Earth-Science Reviews*, *55*(1–2), 1–39. https://doi.org/10.1016/S0012-8252(01)00055-1

Basak, C., & Martin, E. E. (2013). Antarctic weathering and carbonate compensation at the Eocene–Oligocene transition. *Nature Geoscience*, *6*(2), 121–124. https://doi.org/10.1038/ngeo1707

Basak, C., Pahnke, K., Frank, M., Lamy, F., & Gersonde, R. (2015). Neodymium isotopic characterization of Ross Sea Bottom Water and its advection through the southern South Pacific. *Earth and Planetary Science Letters*, *419*, 211–221. https://doi.org/10.1016/j.epsl.2015.03.011

Bijl, P. K., Houben, A. J. P., Hartman, J. D., Pross, J., Salabarnada, A., Escutia, C., & Sangiorgi, F. (2018). Paleoceanography and ice sheet variability offshore Wilkes Land, Antarctica – Part 2: Insights from Oligocene–Miocene dinoflagellate cyst assemblages. *Climate of the Past*, *14*(7), 1015–1033. https://doi.org/10.5194/cp-14-1015-2018

Bostock, H. C., Barrows, T. T., Carter, L., Chase, Z., Cortese, G., Dunbar, G. B., et al. (2013). A review of the Australian–New Zealand sector of the Southern Ocean over the last 30 ka (Aus-INTIMATE project). *Quaternary Science Reviews*, *74*, 35–57. https://doi.org/10.1016/j.quascirev.2012.07.018

Burton, K. W., Ling, H.-F., & O'Nions, R. K. (1997). Closure of the Central American Isthmus and its effect on deep-water formation in the North Atlantic. *Nature*, *386*(6623), 382–385. https://doi.org/10.1038/386382a0

Carter, L., McCave, I. N., & Williams, M. J. M. (2008). Chapter 4 circulation and water masses of the Southern Ocean: A review. In F. Florindo & M. Siegert (Eds.), *Developments in Earth and environmental sciences* (pp. 85–114). Elsevier.

Chen, M., Carrasco, G., Zhao, N., Wang, X., Lee, J. N., Tanzil, J. T. I., et al. (2023). Boundary exchange completes the marine Pb cycle jigsaw. *Proceedings of the National Academy of Sciences of the United States of America*, *120*(6), e2213163120. https://doi.org/10.1073/pnas.2213163120

Chen, T.-Y., Ling, H.-F., Hu, R., Frank, M., & Jiang, S.-Y. (2013). Lead isotope provinciality of central North Pacific Deep Water over the Cenozoic. *Geochemistry, Geophysics, Geosystems*, *14*(5), 1523–1537. https://doi.org/10.1002/ggge.20114

Chmeleff, J., von Blanckenburg, F., Kossert, K., & Jakob, D. (2010). Determination of the ^{10}Be half-life by multicollector ICP-MS and liquid scintillation counting. *Nuclear Instruments and Methods in Physics Research Section B: Beam Interactions with Materials and Atoms*, *268*(2), 192–199. https://doi.org/10.1016/j.nimb.2009.09.012

Christensen, J. N., Halliday, A. N., Godfrey, L. V., Hein, J. R., & Rea, D. K. (1997). Climate and ocean dynamics and the lead isotopic records in Pacific ferromanganese crusts. *Science*, *277*(5328), 913–918. https://doi.org/10.1126/science.277.5328.913

Cochran, J. K., McKibbin-Vaughan, T., Dornblaser, M. M., Hirschberg, D., Livingston, H. D., & Buesseler, K. O. (1990). 210Pb scavenging in the North Atlantic and North Pacific Oceans. *Earth and Planetary Science Letters*, *97*(3–4), 332–352. https://doi.org/10.1016/0012-821X(90)90050-8

Conkright, M. E., Levitus, S., O'Brien, T., Boyer, T. P., Stephens, C., Johnson, D., et al. (1998). *World Ocean database 1998 documentation and quality control*. National Oceanographic Data Center.

Consortium, T. C. C. P. I. P., Hönisch, B., Royer, D. L., Breecker, D. O., Polissar, P. J., Bowen, G. J., et al. (2023). Toward a Cenozoic history of atmospheric CO_2. *Science*, *382*, eadi5177. https://doi.org/10.1126/science.adi5177

Coxall, H. K., Huck, C. E., Huber, M., Lear, C. H., Legarda-Lisarri, A., O'Regan, M., et al. (2018). Export of nutrient rich Northern Component Water preceded earlyOligocene Antarctic glaciation. *Nature Geoscience*, *11*(3), 190–196. https://doi.org/10.1038/s41561-018-0069-9

Crocket, K. C., Vance, D., Foster, G. L., Richards, D. A., & Tranter, M. (2012). Continental weathering fluxes during the last glacial/interglacial cycle: Insights from the marine sedimentary Pb isotope record at Orphan Knoll, NW Atlantic. *Quaternary Science Reviews*, *38*, 89–99. https://doi.org/10.1016/j.quascirev.2012.02.004

Dalziel, I. W. D., Lawver, L. A., Pearce, J. A., Barker, P. F., Hastie, A. R., Barfod, D. N., et al. (2013). A potential barrier to deep Antarctic circumpolar flow until the late Miocene? *Geology*, *41*(9), 947–950. https://doi.org/10.1130/g34352.1

Dausmann, V., Gutjahr, M., Frank, M., Kouzmanov, K., & Schaltegger, U. (2019). Experimental evidence for mineral-controlled release of radiogenic Nd, Hf, and Pb isotopes from granitic rocks during progressive chemical weathering. *Chemical Geology*, *507*, 64–84. https://doi.org/10.1016/j.chemgeo.2018.12.024

DeConto, R. M., Pollard, D., Wilson, P. A., Pälike, H., Lear, C. H., & Pagani, M. (2008). Thresholds for Cenozoic bipolar glaciation. *Nature*, *455*(7213), 652–656. https://doi.org/10.1038/nature07337

Erel, Y., Blum, J. D., Roueff, E., & Ganor, J. (2004). Lead and strontium isotopes as monitors of experimental granitoid mineral dissolution. *Geochimica et Cosmochimica Acta*, *68*(22), 4649–4663. https://doi.org/10.1016/j.gca.2004.04.022

Evangelinos, D., Escutia, C., van de Flierdt, T., Valero, L., Flores, J.-A., Harwood, D. M., et al. (2022). Absence of a strong, deep-reaching Antarctic Circumpolar Current zonal flow across the Tasmanian gateway during the Oligocene to early Miocene. *Global and Planetary Change*, *208*, 103718. https://doi.org/10.1016/j.gloplacha.2021.103718

Evangelinos, D., Etourneau, J., van de Flierdt, T., Crosta, X., Jeandel, C., Flores, J.-A., et al. (2024). Late Miocene onset of the modern Antarctic Circumpolar Current. *Nature Geoscience*, *17*(2), 165–170. https://doi.org/10.1038/s41561-023-01356-3

Farmer, G. L., Licht, K., Swope, R. J., & Andrews, J. (2006). Isotopic constraints on the provenance of fine-grained sediment in LGM tills from the Ross Embayment, Antarctica. *Earth and Planetary Science Letters*, *249*, 90–107. https://doi.org/10.1016/j.epsl.2006.06.044

Flower, B. P., & Kennett, J. P. (1995). Middle Miocene deepwater paleoceanography in the Southwest Pacific: Relations with East Antarctic Ice Sheet development. *Paleoceanography*, *10*(6), 1095–1112. https://doi.org/10.1029/95pa02022

Foster, G. L., Lear, C. H., & Rae, J. W. B. (2012). The evolution of pCO_2, ice volume and climate during the middle Miocene. *Earth and Planetary Science Letters*, *341–344*, 243–254. https://doi.org/10.1016/j.epsl.2012.06.007

Foster, G. L., & Rohling, E. J. (2013). Relationship between sea level and climate forcing by CO_2 on geological timescales. *Proceedings of the National Academy of Sciences of the United States of America*, *110*(4), 1209–1214. https://doi.org/10.1073/pnas.1216073110

Frank, M. (2002). Radiogenic isotopes: Tracers of past ocean circulation and erosional input. *Review of Geophysics*, *40*(1), 1001. https://doi.org/10.1029/2000rg000094

Frank, M., O'Nions, R. K., Hein, J. R., & Banakar, V. K. (1999). 60 Myr records of major elements and Pb–Nd isotopes from hydrogenous ferromanganese crusts: Reconstruction of seawater paleochemistry. *Geochimica et Cosmochimica Acta*, *63*(11–12), 1689–1708. https://doi.org/10.1016/S0016-7037(99)00079-4

Frank, M., Whiteley, N., Kasten, S., Hein, J. R., & O'Nions, K. (2002). North Atlantic Deep Water export to the Southern Ocean over the past 14 Myr: Evidence from Nd and Pb isotopes in ferromanganese crusts. *Paleoceanography*, *17*(2), 1022. https://doi.org/10.1029/2000pa000606

Fyke, J. G., D'Orgeville, M., & Weaver, A. J. (2015). Drake Passage and Central American Seaway controls on the distribution of the oceanic carbon reservoir. *Global and Planetary Change*, *128*, 72–82. https://doi.org/10.1016/j.gloplacha.2015.02.011

Garcia, H. E., Locarnini, R. A., Boyer, T. P., Antonov, J. I., Mishonov, A. V., Baranova, O. K., et al. (2013). Dissolved oxygen, apparent oxygen utilization, and oxygen saturation. In *World Ocean Atlas 2013* (Vol. 3, p. 27).

Gohl, K. (2010). The expedition of the research vessel "polarstern" to the Amundsen Sea, Antarctica, in 2010 (ANT-XXVI/3). Berichte zur Polar-und Meeresforschung (Reports on Polar and Marine Research), Bremerhaven, Alfred Wegener Institute for Polar and Marine Research, *617*, 173. https://doi.org/10.2312/BzPM_0617_2010

Gordon, A. L. (2001). Current systems in the Southern Ocean. In J. H. Steele (Ed.), *Encyclopedia of ocean sciences* (2nd ed., pp. 735–743). Academic Press.

Greenop, R., Foster, G. L., Wilson, P. A., & Lear, C. H. (2014). Middle Miocene climate instability associated with high-amplitude CO_2 variability. *Paleoceanography*, *29*(9), 845–853. https://doi.org/10.1002/2014PA002653

Gulick, S. P. S., Shevenell, A. E., Montelli, A., Fernandez, R., Smith, C., Warny, S., et al. (2017). Initiation and long-term instability of the East Antarctic Ice Sheet. *Nature*, *552*(7684), 225–229. https://doi.org/10.1038/nature25026

Gutjahr, M., Frank, M., Halliday, A. N., & Keigwin, L. D. (2009). Retreat of the Laurentide ice sheet tracked by the isotopic composition of Pb in western North Atlantic seawater during termination 1. *Earth and Planetary Science Letters*, *286*(3–4), 546–555. https://doi.org/10.1016/j.epsl.2009.07.020

Haug, G. H., & Tiedemann, R. (1998). Effect of the formation of the Isthmus of Panama on Atlantic Ocean thermohaline circulation. *Nature*, *393*(6686), 673–676. https://doi.org/10.1038/31447

Haywood, A. M., Dowsett, H. J., Dolan, A. M., Rowley, D., Abe-Ouchi, A., Otto-Bliesner, B., et al. (2016). The Pliocene Model Intercomparison Project (PlioMIP) Phase 2: Scientific objectives and experimental design. *Climate of the Past*, *12*(3), 663–675. https://doi.org/10.5194/cp-12-663-2016

Henderson, G. M., & Maier-Reimer, E. (2002). Advection and removal of ^{210}Pb and stable Pb isotopes in the oceans: A general circulation model study. *Geochimica et Cosmochimica Acta*, *66*(2), 257–272. https://doi.org/10.1016/S0016-7037(01)00779-7

Hillenbrand, C. D., Crowhurst, S. J., Williams, M., Hodell, D. A., McCave, I. N., Ehrmann, W., et al. (2021). New insights from multi-proxy data from the West Antarctic continental rise: Implications for dating and interpreting Late Quaternary palaeoenvironmental records. *Quaternary Science Reviews*, *257*, 106842. https://doi.org/10.1016/j.quascirev.2021.106842

Hillenbrand, C. D., Kuhn, G., & Frederichs, T. (2009). Record of a Mid-Pleistocene depositional anomaly in West Antarctic continental margin sediments: An indicator for ice-sheet collapse? *Quaternary Science Reviews*, *28*(13–14), 1147–1159. https://doi.org/10.1016/j.quascirev.2008.12.010

Hochmuth, K., Gohl, K., Leitchenkov, G., Sauermilch, I., Whittaker, J. M., Uenzelmann-Neben, G., et al. (2020). The evolving paleobathymetry of the circum-Antarctic Southern Ocean since 34 Ma: A key to understanding past cryosphere-ocean developments. *Geochemistry, Geophysics, Geosystems*, *21*(8), e2020GC009122. https://doi.org/10.1029/2020GC009122

Hohbein, M. W., Sexton, P. F., & Cartwright, J. A. (2012). Onset of North Atlantic Deep Water production coincident with inception of the Cenozoic global cooling trend. *Geology*, *40*(3), 255–258. https://doi.org/10.1130/g32461.1

Holbourn, A., Kuhnt, W., Frank, M., & Haley, B. A. (2013). Changes in Pacific Ocean circulation following the Miocene onset of permanent Antarctic ice cover. *Earth and Planetary Science Letters*, *365*, 38–50. https://doi.org/10.1016/j.epsl.2013.01.020

Holbourn, A., Kuhnt, W., Schulz, M., & Erlenkeuser, H. (2005). Impacts of orbital forcing and atmospheric carbon dioxide on Miocene ice-sheet expansion. *Nature*, *438*(7067), 483–487. https://doi.org/10.1038/nature04123

Huang, H., Gutjahr, M., Eisenhauer, A., & Kuhn, G. (2020). No detectable Weddell Sea Antarctic Bottom Water export during the last and penultimate glacial maximum. *Nature Communications*, *11*(1), 424. https://doi.org/10.1038/s41467-020-14302-3

Huang, H., Gutjahr, M., Song, Z., Fietzke, J., Frank, M., Kuhn, G., et al. (2024). Pb isotope composition in the ferromanganese crust PS75/247-2 [Dataset]. PANGAEA. https://doi.org/10.1594/PANGAEA.973140

Inoue, T., Huang, Z.-Y., Imamura, M., Tanaka, S., & Usui, A. (1983). ^{10}Be and ^{10}Be/9Be in manganese nodules. *Geochemical Journal*, *17*(6), 307–312. https://doi.org/10.2343/geochemj.17.307

Karas, C., Nürnberg, D., Bahr, A., Groeneveld, J., Herrle, J. O., Tiedemann, R., & deMenocal, P. B. (2017). Pliocene oceanic seaways and global climate. *Scientific Reports*, *7*(1), 39842. https://doi.org/10.1038/srep39842

Karas, C., Nürnberg, D., Tiedemann, R., & Garbe-Schönberg, D. (2011). Pliocene climate change of the Southwest Pacific and the impact of ocean gateways. *Earth and Planetary Science Letters*, *301*(1–2), 117–124. https://doi.org/10.1016/j.epsl.2010.10.028

Kennett, J. P. (1977). Cenozoic evolution of Antarctic glaciation, the circum-Antarctic Ocean, and their impact on global paleoceanography. *Journal of Geophysical Research (1896-1977)*, *82*(27), 3843–3860. https://doi.org/10.1029/JC082i027p03843

Kennett, J. P. (1985). *The Miocene ocean: Paleoceanography and biogeography* (p. 343). Geological Society of America.

Kennett, J. P., & Barker, P. F. (1990). Latest cretaceous to Cenozoic climate and oceanographic developments in the Weddell Sea, Antarctica: An ocean-drilling perspective.

Kennett, J. P., Gerta, K., & Srinivasan, M. S. (1985). Miocene planktonic foraminiferal biogeography and paleoceanographic development of the Indo-Pacific region. In *Geological society of America memoirs*. Geological Society of America.

Kipf, A., Hauff, F., Werner, R., Gohl, K., van den Bogaard, P., Hoernle, K., et al. (2014). Seamounts off the West Antarctic margin: A case for non-hotspot driven intraplate volcanism. *Gondwana Research*, *25*(4), 1660–1679. https://doi.org/10.1016/j.gr.2013.06.013

Kirillova, V., Osborne, A. H., Störling, T., & Frank, M. (2019). Miocene restriction of the Pacific-North Atlantic throughflow strengthened Atlantic overturning circulation. *Nature Communications*, *10*(1), 4025. https://doi.org/10.1038/s41467-019-12034-7

Klemm, V., Reynolds, B., Frank, M., Pettke, T., & Halliday, A. N. (2007). Cenozoic changes in atmospheric lead recorded in central Pacific ferromanganese crusts. *Earth and Planetary Science Letters*, *253*(1–2), 57–66. https://doi.org/10.1016/j.epsl.2006.10.018

Knorr, G., & Lohmann, G. (2014). Climate warming during Antarctic ice sheet expansion at the Middle Miocene transition. *Nature Geoscience*, *7*(5), 376–381. https://doi.org/10.1038/ngeo2119

Kurzweil, F., Gutjahr, M., Vance, D., & Keigwin, L. (2010). Authigenic Pb isotopes from the Laurentian Fan: Changes in chemical weathering and patterns of North American freshwater runoff during the last deglaciation. *Earth and Planetary Science Letters*, *299*(3–4), 458–465. https://doi.org/10.1016/j.epsl.2010.09.031

Lambelet, M., van de Flierdt, T., Butler, E. C. V., Bowie, A. R., Rintoul, S. R., Watson, R. J., et al. (2018). The neodymium isotope fingerprint of Adélie Coast Bottom Water. *Geophysical Research Letters*, *45*(20), 11247–211256. https://doi.org/10.1029/2018gl080074

Lamy, F., Gersonde, R., Winckler, G., Esper, O., Jaeschke, A., Kuhn, G., et al. (2014). Increased dust deposition in the Pacific Southern Ocean during glacial periods. *Science*, *343*(6169), 403–407. https://doi.org/10.1126/science.1245424

Lanning, N. T., Jiang, S., Amaral, V. J., Mateos, K., Steffen, J. M., Lam, P. J., et al. (2023). Isotopes illustrate vertical transport of anthropogenic Pb by reversible scavenging within Pacific Ocean particle veils. *Proceedings of the National Academy of Sciences of the United States of America*, *120*(23), e2219688120. https://doi.org/10.1073/pnas.2219688120

Lawver, L. A., & Gahagan, L. M. (2003). Evolution of Cenozoic seaways in the circum-Antarctic region. *Palaeogeography, Palaeoclimatology, Palaeoecology*, *198*(1–2), 11–37. https://doi.org/10.1016/S0031-0182(03)00392-4

Levy, R., Harwood, D., Florindo, F., Sangiorgi, F., Tripati, R., von Eynatten, H., et al. (2016). Antarctic ice sheet sensitivity to atmospheric CO_2 variations in the early to mid-Miocene. *Proceedings of the National Academy of Sciences of the United States of America*, *113*(13), 3453–3458. https://doi.org/10.1073/pnas.1516030113

Livermore, R., Nankivell, A., Eagles, G., & Morris, P. (2005). Paleogene opening of Drake Passage. *Earth and Planetary Science Letters*, *236*(1–2), 459–470. https://doi.org/10.1016/j.epsl.2005.03.027

Lumpkin, R., & Speer, K. (2007). Global Ocean meridional overturning. *Journal of Physical Oceanography*, *37*(10), 2550–2562. https://doi.org/10.1175/JPO3130.1

Lüthi, D., Le Floch, M., Bereiter, B., Blunier, T., Barnola, J.-M., Siegenthaler, U., et al. (2008). High-resolution carbon dioxide concentration record 650,000–800,000 years before present. *Nature*, *453*(7193), 379–382. https://doi.org/10.1038/nature06949

Ma, X., Tian, J., Ma, W., Li, K., & Yu, J. (2018). Changes of deep Pacific overturning circulation and carbonate chemistry during middle Miocene East Antarctic ice sheet expansion. *Earth and Planetary Science Letters*, *484*, 253–263. https://doi.org/10.1016/j.epsl.2017.12.002

Madec, G. (2008). NEMO ocean engine. Note du Pole de modélisation 27, Institut Pierre-Simon Laplace, 193.

Mahowald, N., Albani, S., Engelstaedter, S., Winckler, G., & Goman, M. (2011). Model insight into glacial–interglacial paleodust records. *Quaternary Science Reviews*, *30*(7–8), 832–854. https://doi.org/10.1016/j.quascirev.2010.09.007

Manheim, F. T. (1986). Marine cobalt resources. *Science*, *232*(4750), 600–608. https://doi.org/10.1126/science.232.4750.600

Marsay, C. M., Aguilar-Islas, A., Fitzsimmons, J. N., Hatta, M., Jensen, L. T., John, S. G., et al. (2018). Dissolved and particulate trace elements in late summer Arctic melt ponds. *Marine Chemistry*, *204*, 70–85. https://doi.org/10.1016/j.marchem.2018.06.002

Marschalek, J. W., Zurli, L., Talarico, F., van de Flierdt, T., Vermeesch, P., Carter, A., et al. (2021). A large West Antarctic Ice Sheet explains early Neogene sea-level amplitude. *Nature*, *600*(7889), 450–455. https://doi.org/10.1038/s41586-021-04148-0

Miller, K. G., Browning, J. V., Schmelz, W. J., Kopp, R. E., Mountain, G. S., & Wright, J. D. (2020). Cenozoic sea-level and cryospheric evolution from deep-sea geochemical and continental margin records. *Science Advances*, *6*(20), eaaz1346. https://doi.org/10.1126/sciadv.aaz1346

Molina-Kescher, M., Frank, M., Tapia, R., Ronge, T. A., Nürnberg, D., & Tiedemann, R. (2016). Reduced admixture of North Atlantic Deep Water to the deep central South Pacific during the last two glacial periods. *Paleoceanography and Paleoclimatology*, *31*(6), 651–668. https://doi.org/10.1002/2015PA002863

Naish, T., Powell, R., Levy, R., Wilson, G., Scherer, R., Talarico, F., et al. (2009). Obliquity-paced Pliocene West Antarctic ice sheet oscillations. *Nature*, *458*(7236), 322–328. https://doi.org/10.1038/nature07867

Ndungu, K., Zurbrick, C. M., Stammerjohn, S., Severmann, S., Sherrell, R. M., & Flegal, A. R. (2016). Lead sources to the Amundsen Sea, west Antarctica. *Environmental Science & Technology*, *50*(12), 6233–6239. https://doi.org/10.1021/acs.est.5b05151

Nishimura, S., & Suparka, S. (1997). Tectonic approach to the Neogene evolution of Pacific-Indian Ocean seaways. *Tectonophysics*, *281*(1–2), 1–16. https://doi.org/10.1016/S0040-1951(97)00155-8

Orsi, A. H., Johnson, G. C., & Bullister, J. L. (1999). Circulation, mixing, and production of Antarctic Bottom Water. *Progress in Oceanography*, *43*(1), 55–109. https://doi.org/10.1016/S0079-6611(99)00004-X

Orsi, A. H., Whitworth, T., & Nowlin, W. D. (1995). On the meridional extent and fronts of the Antarctic Circumpolar Current. *Deep-Sea Research Part I Oceanographic Research Papers*, *42*(5), 641–673. https://doi.org/10.1016/0967-0637(95)00021-W

Park, W., Keenlyside, N., Latif, M., Ströh, A., Redler, R., Roeckner, E., & Madec, G. (2009). Tropical Pacific climate and its response to global warming in the Kiel climate model. *Journal of Climate*, *22*(1), 71–92. https://doi.org/10.1175/2008JCLI2261.1

Pérez, L. F., McKay, R. M., De Santis, L., Larter, R. D., Levy, R. H., Naish, T. R., et al. (2022). Early to middle Miocene ice sheet dynamics in the westernmost Ross Sea (Antarctica): Regional correlations. *Global and Planetary Change*, *216*, 103891. https://doi.org/10.1016/j.gloplacha.2022.103891

Pfuhl, H. A., & McCave, I. N. (2005). Evidence for late Oligocene establishment of the Antarctic Circumpolar Current. *Earth and Planetary Science Letters*, *235*(3–4), 715–728. https://doi.org/10.1016/j.epsl.2005.04.025

Purkey, S. G., Smethie, W. M., Gebbie, G., Gordon, A. L., Sonnerup, R. E., Warner, M. J., & Bullister, J. L. (2018). A synoptic view of the ventilation and circulation of Antarctic Bottom Water from chlorofluorocarbons and natural tracers. *Annual Review of Marine Science*, *10*(1), 503–527. https://doi.org/10.1146/annurev-marine-121916-063414

Rae, J. W. B., Zhang, Y. G., Liu, X., Foster, G. L., Stoll, H. M., & Whiteford, R. D. M. (2021). Atmospheric CO_2 over the past 66 million years from marine archives. *Annual Review of Earth and Planetary Sciences*, *49*(1), 609–641. https://doi.org/10.1146/annurev-earth-082420-063026

Raymo, M. E., Hodell, D., & Jansen, E. (1992). Response of deep ocean circulation to initiation of northern hemisphere glaciation (3–2 MA). *Paleoceanography*, *7*(5), 645–672. https://doi.org/10.1029/92pa01609

Rickli, J., Gutjahr, M., Vance, D., Fischer-Gödde, M., Hillenbrand, C.-D., & Kuhn, G. (2014). Neodymium and hafnium boundary contributions to seawater along the West Antarctic continental margin. *Earth and Planetary Science Letters*, *394*, 99–110. https://doi.org/10.1016/j.epsl.2014.03.008

Riley, T. R., Burton-Johnson, A., Leat, P. T., Hogan, K. A., & Halton, A. M. (2021). Geochronology and geochemistry of the South Scotia Ridge: Miocene island arc volcanism of the Scotia Sea. *Global and Planetary Change*, *205*, 103615. https://doi.org/10.1016/j.gloplacha.2021.103615

Rintoul, S. R. (2018). The global influence of localized dynamics in the Southern Ocean. *Nature*, *558*(7709), 209–218. https://doi.org/10.1038/s41586-018-0182-3

Roeckner, E., Bäuml, G., Bonaventura, L., Brokopf, R., Esch, M., & Giorgetta, M. (2003). The atmospheric general circulation model ECHAM 5. PART I: Model description. Report / Max-Planck-Institut für Meteorologie.

Ruddiman, W. F., McIntyre, A., Niebler-Hunt, V., & Durazzi, J. T. (2017). Oceanic evidence for the mechanism of rapid northern hemisphere glaciation. *Quaternary Research*, *13*(1), 33–64. https://doi.org/10.1016/0033-5894(80)90081-2

Sangiorgi, F., Bijl, P. K., Passchier, S., Salzmann, U., Schouten, S., McKay, R., et al. (2018). Southern Ocean warming and Wilkes Land ice sheet retreat during the mid-Miocene. *Nature Communications*, *9*(1), 317. https://doi.org/10.1038/s41467-017-02609-7

Sauermilch, I., Whittaker, J. M., Klocker, A., Munday, D. R., Hochmuth, K., Bijl, P. K., & LaCasce, J. H. (2021). Gateway-driven weakening of ocean gyres leads to Southern Ocean cooling. *Nature Communications*, *12*(1), 6465. https://doi.org/10.1038/s41467-021-26658-1

Schaule, B. K., & Patterson, C. C. (1981). Lead concentrations in the northeast Pacific: Evidence for global anthropogenic perturbations. *Earth and Planetary Science Letters*, *54*(1), 97–116. https://doi.org/10.1016/0012-821X(81)90072-8

Scher, H. D., & Martin, E. E. (2006). Timing and climatic consequences of the opening of Drake Passage. *Science*, *312*(5772), 428–430. https://doi.org/10.1126/science.1120044

Scher, H. D., Whittaker, J. M., Williams, S. E., Latimer, J. C., Kordesch, W. E. C., & Delaney, M. L. (2015). Onset of Antarctic Circumpolar Current 30 million years ago as Tasmanian Gateway aligned with westerlies. *Nature*, *523*(7562), 580–583. https://doi.org/10.1038/nature14598

Schlitzer, R. (2011). Ocean data view. http://odv.awi.de

Shackleton, N. J., & Opdyke, N. D. (1977). Oxygen isotope and palaeomagnetic evidence for early Northern Hemisphere glaciation. *Nature*, *270*(5634), 216–219. https://doi.org/10.1038/270216a0

Shevenell, A. E., Kennett, J. P., & Lea, D. W. (2008). Middle Miocene ice sheet dynamics, deep-sea temperatures, and carbon cycling: A Southern Ocean perspective. *Geochemistry, Geophysics, Geosystems*, *9*(2), Q02006. https://doi.org/10.1029/2007GC001736

Shevenell, A. E., Kennett, J. P., & Lea David, W. (2004). Middle Miocene Southern Ocean cooling and Antarctic cryosphere expansion. *Science*, *305*(5691), 1766–1770. https://doi.org/10.1126/science.1100061

Simões Pereira, P., van de Flierdt, T., Hemming, S. R., Hammond, S. J., Kuhn, G., Brachfeld, S., et al. (2018). Geochemical fingerprints of glacially eroded bedrock from West Antarctica: Detrital thermochronology, radiogenic isotope systematics and trace element geochemistry in Late Holocene glacial-marine sediments. *Earth-Science Reviews*, *182*, 204–232. https://doi.org/10.1016/j.earscirev.2018.04.011

Solodoch, A., Stewart, A. L., Hogg, A. M., Morrison, A. K., Kiss, A. E., Thompson, A. F., et al. (2022). How does Antarctic Bottom Water cross the Southern Ocean? *Geophysical Research Letters*, *49*(7), e2021GL097211. https://doi.org/10.1029/2021GL097211

Song, Z., Latif, M., Park, W., Krebs-Kanzow, U., & Schneider, B. (2017). Influence of seaway changes during the Pliocene on tropical Pacific climate in the Kiel climate model: Mean state, annual cycle, ENSO, and their interactions. *Climate Dynamics*, *48*(11–12), 3725–3740. https://doi.org/10.1007/s00382-016-3298-x

Stickley, C. E., Brinkhuis, H., Schellenberg, S. A., Sluijs, A., Röhl, U., Fuller, M., et al. (2004). Timing and nature of the deepening of the Tasmanian Gateway. *Paleoceanography*, *19*(4), PA4027. https://doi.org/10.1029/2004pa001022

Struve, T., Pahnke, K., Lamy, F., Wengler, M., Böning, P., & Winckler, G. (2020). A circumpolar dust conveyor in the glacial Southern Ocean. *Nature Communications*, *11*(1), 5655. https://doi.org/10.1038/s41467-020-18858-y

Talley, L. D. (2013). Closure of the global overturning circulation through the Indian, Pacific, and southern oceans: Schematics and transports. *Oceanography*, *26*(1), 80–97. https://doi.org/10.5670/oceanog.2013.07

Thomas, G., Purkey, S. G., Roemmich, D., Foppert, A., & Rintoul, S. R. (2020). Spatial variability of Antarctic Bottom Water in the Australian Antarctic Basin from 2018–2020 captured by deep argo. *Geophysical Research Letters*, *47*(23), e2020GL089467. https://doi.org/10.1029/2020GL089467

Toulouse, F., van de Flierdt, T., Frank, M., Halliday, A. N., Hein, J. R., Hattendorf, B., et al. (2004). Deep and bottom water export from the Southern Ocean to the Pacific over the past 38 million years. *Paleoceanography*, *19*(1), PA1020. https://doi.org/10.1029/2003pa000923

Valcke, S. (2006). OASIS3 user Guide (PRISM_2–5). CERFACS Technical Report TR/CMGC/06/73, PRISM Report No 3 (p. 60).

van de Flierdt, T., Frank, M., Halliday, A. N., Hein, J. R., Hattendorf, B., Günther, D., & Kubik, P. W. (2004). Deep and bottom water export from the Southern Ocean to the Pacific over the past 38 million years. *Paleoceanography*, *19*(1), PA1020. https://doi.org/10.1029/2003pa000923

van de Flierdt, T., Griffiths, A. M., Lambelet, M., Little, S. H., Stichel, T., & Wilson, D. J. (2016). Neodymium in the oceans: A global database, a regional comparison and implications for palaeoceanographic research. *Philosophical Transactions of the Royal Society A: Mathematical, Physical and Engineering Sciences*, *374*(2081), 20150293. https://doi.org/10.1098/rsta.2015.0293

van de Lagemaat, S. H. A., Swart, M. L. A., Vaes, B., Kosters, M. E., Boschman, L. M., Burton-Johnson, A., et al. (2021). Subduction initiation in the Scotia Sea region and opening of the Drake Passage: When and why? *Earth-Science Reviews*, *215*, 103551. https://doi.org/10.1016/j.earscirev.2021.103551

Vincent, E., Killingley, J. S., & Berger, W. H. (1985). Miocene oxygen and carbon isotope stratigraphy of the tropical Indian Ocean. *Geological Society of America Memoirs*, 103–130. https://doi.org/10.1130/mem163-p103

von Blanckenburg, F., O'Nions, R. K., & Heinz, J. R. (1996). Distribution and sources of pre-anthropogenic lead isotopes in deep ocean water from FeMn crusts. *Geochimica et Cosmochimica Acta*, *60*, 4957–4963. https://doi.org/10.1016/S0016-7037(96)00310-9

Wåhlin, A. K., Kalén, O., Arneborg, L., Björk, G., Carvajal, G. K., Ha, H. K., et al. (2013). Variability of warm deep water inflow in a submarine trough on the Amundsen Sea shelf. *Journal of Physical Oceanography*, *43*(10), 2054–2070. https://doi.org/10.1175/JPO-D-12-0157.1

Wang, H., Liu, W., Lu, H., Zhang, Y., Liang, Y., He, Y., et al. (2023). Oxygenated deep waters fed early Atlantic overturning circulation upon Antarctic glaciation. *Nature Geoscience*, *16*, 1014–1019. https://doi.org/10.1038/s41561-023-01292-2

Wengler, M., Lamy, F., Struve, T., Borunda, A., Böning, P., Geibert, W., et al. (2019). A geochemical approach to reconstruct modern dust fluxes and sources to the South Pacific. *Geochimica et Cosmochimica Acta*, *264*, 205–223. https://doi.org/10.1016/j.gca.2019.08.024

Woodruff, F., & Savin, S. M. (1989). Miocene deepwater oceanography. *Paleoceanography*, *4*(1), 87–140. https://doi.org/10.1029/PA004i001p00087

Wu, J., Rember, R., Jin, M., Boyle, E. A., & Flegal, A. R. (2010). Isotopic evidence for the source of lead in the North Pacific abyssal water. *Geochimica et Cosmochimica Acta*, *74*(16), 4629–4638. https://doi.org/10.1016/j.gca.2010.05.017

Zachos, J., Pagani, M., Sloan, L., Thomas, E., & Billups, K. (2001). Trends, rhythms, and aberrations in global climate 65 Ma to present. *Science*, *292*(5517), 686–693. https://doi.org/10.1126/science.1059412

Zhang, X., Prange, M., Steph, S., Butzin, M., Krebs, U., Lunt, D. J., et al. (2012). Changes in equatorial Pacific thermocline depth in response to Panamanian seaway closure: Insights from a multi-model study. *Earth and Planetary Science Letters*, *317–318*, 76–84. https://doi.org/10.1016/j.epsl.2011.11.028

Zhang, Y. G., Pagani, M., Liu, Z., Bohaty, S. M., & DeConto, R. (2013). A 40-million-year history of atmospheric CO_2. *Philosophical Transactions of the Royal Society A: Mathematical, Physical and Engineering Sciences*, *371*(2001), 20130096. https://doi.org/10.1098/rsta.2013.0096

Zweng, M. M., Reagan, J. R., Antonov, J. I., Locarnini, R. A., Mishonov, A. V., Boyer, T. P., et al. (2013). Salinity. In *World Ocean Atlas 2013* (Vol. 2).

References From the Supporting Information

Baker, J., Peate, D., Waight, T., & Meyzen, C. (2004). Pb isotopic analysis of standards and samples using a 207Pb–204Pb double spike and thallium to correct for mass bias with a double-focusing MC-ICP-MS. *Chemical Geology*, *211*(3–4), 275–303. https://doi.org/10.1016/j.chemgeo.2004.06.030

Belshaw, N. S., Freedman, P. A., O'Nions, R. K., Frank, M., & Guo, Y. (1998). A new variable dispersion double-focusing plasma mass spectrometer with performance illustrated for Pb isotopes. *International Journal of Mass Spectrometry*, *181*(1–3), 51–58. https://doi.org/10.1016/S1387-3806(98)14150-7

Christl, M., Vockenhuber, C., Kubik, P. W., Wacker, L., Lachner, J., Alfimov, V., & Synal, H. A. (2013). The ETH Zurich AMS facilities: Performance parameters and reference materials. *Nuclear Instruments and Methods in Physics Research Section B: Beam Interactions with Materials and Atoms*, *294*, 29–38. https://doi.org/10.1016/j.nimb.2012.03.004

Fietzke, J., & Frische, M. (2016). Experimental evaluation of elemental behavior during LA-ICP-MS: Influences of plasma conditions and limits of plasma robustness. *Journal of Analytical Atomic Spectrometry*, *31*(1), 234–244. https://doi.org/10.1039/C5JA00253B

Fietzke, J., Liebetrau, V., Günther, D., Gürs, K., Hametner, K., Zumholz, K., et al. (2008). An alternative data acquisition and evaluation strategy for improved isotope ratio precision using LA-MC-ICP-MS applied to stable and radiogenic strontium isotopes in carbonates. *Journal of Analytical Atomic Spectrometry*, *23*(7), 955–961. https://doi.org/10.1039/B717706B

Frank, M., Eckhardt, J.-D., Eisenhauer, A., Kubik, P. W., Dittrich-Hannen, B., Segl, M., & Mangini, A. (1994). Beryllium 10, thorium 230, and protactinium 231 in Galapagos microplate sediments: Implications of hydrothermal activity and paleoproductivity changes during the last 100,000 years. *Paleoceanography*, *9*(4), 559–578. https://doi.org/10.1029/94pa01132

Garbe-Schönberg, C.-D. (1993). Simultaneous determination of thirty-seven trace elements in twenty-eight international rock standards by ICP-MS. *Geostandards Newsletter*, *17*(1), 81–97. https://doi.org/10.1111/j.1751-908X.1993.tb00122.x

Henken-Mellies, W. U., Beer, J., Heller, F., Hsü, K. J., Shen, C., Bonani, G., et al. (1990). 10Be and 9Be in South Atlantic DSDP Site 519: Relation to geomagnetic reversals and to sediment composition. *Earth and Planetary Science Letters*, *98*(3–4), 267–276. https://doi.org/10.1016/0012-821X(90)90029-W

Lugmair, G. W., & Galer, S. J. G. (1992). Age and isotopic relationships among the angrites Lewis Cliff 86010 and Angra dos Reis. *Geochimica et Cosmochimica Acta*, *56*(4), 1673–1694. https://doi.org/10.1016/0016-7037(92)90234-a

Nishiizumi, K., Imamura, M., Caffee, M. W., Southon, J. R., Finkel, R. C., & McAninch, J. (2007). Absolute calibration of 10Be AMS standards. *Nuclear Instruments and Methods in Physics Research Section B: Beam Interactions with Materials and Atoms*, *258*(2), 403–413. https://doi.org/10.1016/j.nimb.2007.01.297

Thirlwall, M. F. (2002). Multicollector ICP-MS analysis of Pb isotopes using a 207Pb-204Pb double spike demonstrates up to 400 ppm/amu systematic errors in Tl-normalization. *Chemical Geology*, *184*(3–4), 255–279. https://doi.org/10.1016/S0009-2541(01)00365-5